Bennu regolith mobilized by TAGSAM: Expectations for the OSIRIS-REx sample collection event and application to understanding naturally ejected particles

Icarus 355 (2021) 114142

Contents lists available at ScienceDirect

Icarus

journal homepage: www.elsevier.com/locate/icarus

Bennu regolith mobilized by TAGSAM: Expectations for the OSIRIS-REx sample collection event and application to understanding naturally ejected particles

E.B. Bierhaus [a,*], J.T. Songer [a], B.C. Clark [a,b], R.D. Dubisher [a], S.L. Deden [a], K.S. Payne [a], D. Wurts [a], J.W. McMahon [c], B. Rozitis [d], D.S. Lauretta [e]

[a] Lockheed Martin Space, Littleton, CO, USA
[b] Space Science Institute, Boulder, CO, USA
[c] University of Colorado, Boulder, CO, USA
[d] The Open University, Milton Keynes, UK
[e] Lunar and Planetary Laboratory, University of Arizona, Tucson, AZ, USA

ARTICLE INFO

Keywords:
Asteroid Bennu
Experimental techniques
Geological processes
Regoliths

ABSTRACT

The Origins, Spectral Interpretation, Resource Identification, and Security–Regolith Explorer (OSIRIS-REx) mission will collect material from the asteroid Bennu and return it to Earth. The sample collection method uses pressurized nitrogen gas to mobilize regolith. It is likely that the gas will mobilize more, potentially much more, material than is captured by the Touch-and-Go Sample Acquisition Mechanism (TAGSAM) for return. The amount, velocities, and fate of this mobilized material have important implications for our understanding of Bennu's physical properties and processes, such as impact cratering, regolith mobility, and the recently observed natural ejection of particles. The nature of the TAGSAM-ejected material is also significant for mission operations. We conducted numerical simulations and ground-based tests to estimate the amount and speeds of material mobilized by the sampling event. The estimated ejected masses range from 12 kg to >165 kg; given that Bennu appears to be a nearly strengthless rubble pile, the higher end of the mass range is more likely. Maximum ejection speeds for 1-cm-diameter particles could reach 10 m/s; smaller particles will be ejected at faster speeds. Minimum ejection speeds will be determined by the as yet unknown cohesive strength of Bennu's regolith. Material ejected more slowly than 10 cm/s will reaccrete on Bennu; material ejected between 10 and 30 cm/s may or may not reaccrete; and material ejected faster than 30 cm/s will escape. Some of the ejected material is predicted to remain in transient orbits around Bennu. The lifetimes of these orbits span from days to several weeks, the maximum duration of our integrations. Reaccreted material should be concentrated in a region near the sample site, although re-impacts will occur globally. Gas from TAGSAM will mobilize material beyond the contact perimeter; because of interactions between cohesion and microgravity, there is a preferred particle size of mobility, predicted to be tens of centimeters, depending on the TAG latitude. Observing Bennu during and after the sampling event will make it possible to test these predictions and understand how the asteroid responds to disruption and particle mobility across the surface.

1. Introduction

The OSIRIS-REx mission will collect material from the near-Earth asteroid (101955) Bennu to return to Earth for analysis (Lauretta et al., 2017). The sample collection device, called the Touch-And-Go Sample Acquisition Mechanism (TAGSAM), mobilizes material via pressurized gas (Clark et al., 2016; Bierhaus et al., 2018). TAGSAM consists of an arm with a telescoping spring, three pressurized bottles containing curation-grade nitrogen-grade gas, the sampler "head" at the end of the arm that contacts Bennu's surface to collect material, and supporting cabling, motors, valves, and sensors. The expansion of the gas will mobilize material beyond the contact perimeter of TAGSAM, ejecting particles from the surface.

During development of the OSIRIS-REx spacecraft, we conducted

* Corresponding author.
E-mail address: edward.b.bierhaus@lmco.com (E.B. Bierhaus).

https://doi.org/10.1016/j.icarus.2020.114142
Received 1 April 2020; Received in revised form 29 September 2020; Accepted 1 October 2020
Available online 5 October 2020

experiments to understand the dynamics of regolith particles mobilized by TAGSAM to evaluate any risks to the spacecraft and understand the post–sampling event environment around the asteroid. Additional work took place prior to the selection of the OSIRIS-REx primary and backup sample sites, Nightingale and Osprey, respectively (Fig. 1). In Section 4.1, we describe the implication of our results for those locations. For example, any ejected material that reaches orbit around Bennu has operational consequences for subsequent phases of the mission.

In December 2018, the OSIRIS-REx spacecraft reached Bennu and measured its shape (Barnouin et al., 2019), mass, bulk density (Scheeres et al., 2019), and albedo (DellaGiustina et al., 2019; Lauretta et al., 2019a). McMahon et al. (2020) utilize these values to model the evolution of simulated particles ejected under the conditions described in Lauretta et al. (2019b). The McMahon et al. (2020) analysis uses a higher-fidelity treatment of Bennu and non-gravitational forces than this manuscript, whereas the analysis reported here uses a higher-fidelity treatment of particle mass-velocity ejection distributions. (We use "mass-velocity distribution" as that is a community-standard phrase, and indeed, there is some relation between ejection speed and ejection angle for early ejecta, see Anderson et al. (2003). Assuming most ejecta leaves at a 45° ejection angle, a perhaps more appropriate phrase is mass-speed distribution, where the ejection angle is relatively stable, and the major change to the velocity is the velocity magnitude, i.e. speed.)

Prior to OSIRIS-REx's encounter with Bennu, several processes had been proposed that naturally lift and eject material from Bennu's surface, including impact cratering, perhaps electrostatic levitation Colwell et al. (2005); Hartzell and Scheeres (2011), and boulder migration across the surface (Brack and McMahon, 2019). Shortly after the start of orbital operations around Bennu in January 2019, a navigation camera aboard the OSIRIS-REx spacecraft imaged particles leaving Bennu's surface, ejected by natural mechanisms (Lauretta et al., 2019b). Possible mechanisms of ejection include thermal fracturing (Molaro et al., 2020; Molaro et al., 2020a) and meteoroid impacts (Bottke et al., 2020), among others.

Here we describe the analytical and test techniques we developed to estimate the amount and dynamics of material mobilized by the sample collection event, and how these same techniques provide a framework for evaluating the mechanisms and dynamics of natural particle ejections.

There are three over-arching velocity-magnitude regimes for regolith particles ejected from Bennu, based on the relative magnitudes of the ejection velocity v_{ej} and the escape velocity v_{esc} (Fig. 2). The classical escape speed is $v_{esc} = \sqrt{2GM_B/R_B}$, where G is the gravitational constant, M_B is Bennu's mass, and R_B is Bennu's radius. For M_B of 7.329×10^{10} kg and R_B of 245 m (Lauretta et al., 2019a) the classical escape speed is 0.2 m/s. (i) For v_{ej} less than v_{esc}, the particle follows a ballistic trajectory and re-impacts the surface. (ii) For v_{ej} values near v_{esc}, there are non-gravitational perturbing forces, such as solar radiation pressure (SRP), that affect particle trajectories with sufficient magnitude that some particles achieve orbit that would otherwise re-impact or escape. Scheeres (2012) provides a comprehensive discussion of the behaviors and dynamics that affect objects orbiting small bodies. Though the perturbing force is different, this complex behavior of ejecta launched near v_{ej} is comparable to simulations of crater ejecta from Galilean satellites (Alvarellos et al., 2002), Saturnian satellites (Alvarellos et al., 2005), and Pluto and Charon (Bierhaus and Dones, 2015). In those cases, multi-body gravitational effects introduced the dynamically complicated behavior. (iii) Finally, for v_{ej} values above v_{esc}, particles escape the gravitational influence of Bennu and reach independent heliocentric orbits. These same three regimes are used to understand the dynamics of Bennu's naturally ejected particles (McMahon et al., 2020; Chesley et al., 2020; Scheeres et al., 2020; Lauretta et al., 2019b).

All three velocity-magnitude regimes are of interest. Tracking the material that ballistically re-accretes on Bennu's surface illuminates the nature of potential surface disturbances caused by the TAG event beyond the contact location. Understanding the conditions, likelihood, and dynamics of particles that reach orbit — such as likely orbital trajectories and trajectory lifetimes — is needed for post-sampling asteroid operations, and provides a means to test models that evaluate the natural ejection described in Lauretta et al. (2019b). Knowing the transition speed between direct escape and a potentially captured trajectory enables us to estimate the amount of mass that could reside in both temporary and long-term orbits after sampling. Collectively, these data will further inform our understanding of the naturally ejected particles, which also reaccrete on, orbit, and escape from Bennu.

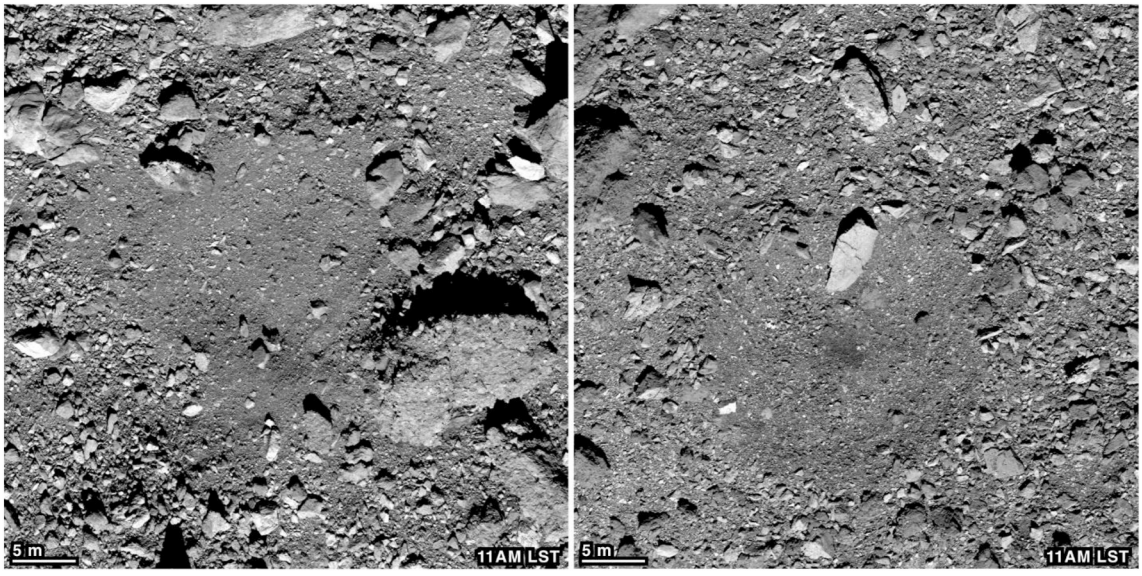

Fig. 1. The left image is Nightingale (56.0° N, 42.1° E), the primary sample site, and the right image is Osprey (11.6° N, 88.9° E), the backup sample site. Both sample sites are inside craters; the Nightingale crater is ~24 m diameter, the Osprey crater is ~21 m diameter. Images were acquired at around 11 am local solar time (LST) for each site. Because Nightingale is at higher latitude, the shadows are longer for the same time of day.

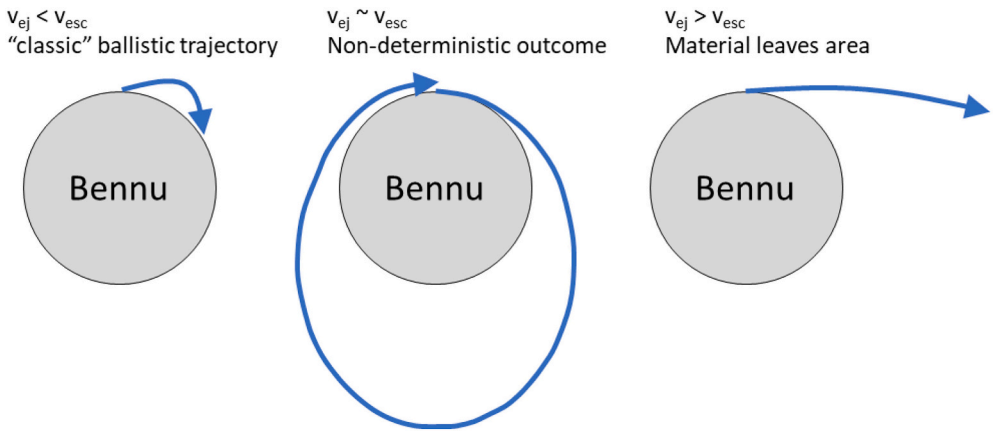

Fig. 2. The three possible outcomes for a particle ejected from Bennu's surface, in order of increasing speed from left to right. Particles ejected well under the escape speed will ballistically re-impact Bennu's surface. Particles ejected near the escape speed may achieve orbit around Bennu. Particles ejected well above the escape speed will escape.

2. Ground testing and simulation of ejecta initial conditions and particle mobility

To evaluate the extent and dynamics of material mobilized by TAGSAM, we applied complementary approaches, combining analytical development and experimental tests. The logic for these tasks was as follows: first, determine the range of particle trajectories (positions, velocities) experienced by particles mobilized by the sample event; this same analysis provides a basis to estimate how much material could be mobilized. Second, use those initial conditions to model the particle trajectories after departure from Bennu's surface and provide insight into the material present in the three velocity-magnitude regimes of interest.

To determine the initial conditions of particle trajectories, we used a combination of numerical simulations and tests. Ground-based testing and observations from tests conducted in low-acceleration environments experienced in parabolic airplane flights provided data to anchor and inform the numerical simulations. The numerical simulations modeled the release of the TAGSAM gas, in particular the pressure/velocity environment immediately outside the TAGSAM head. The remainder of this section describes the testing and complementary analysis.

2.1. Particles mobilized by first contact

There will be a short delay of ~1 s between the initial contact of TAGSAM with Bennu's surface and the release of the pressurized gas for sample collection. In that window of time, the TAGSAM contact transfers energy and momentum into the regolith. Observations from reduced-gravity testing (described below) and simulations confirm the transfer of momentum at contact. Thus, at the time of gas firing, particles ejected from the surface in this manner will surround TAGSAM. This environment sets up the initial conditions for evaluating the dynamics of particles at the time of gas firing. Although the mass mobilized by this first contact is small relative to the total amount ejected by TAGSAM, the behavior is relevant to understand the full range of particle initial conditions at the time of gas release, with implications for potential particle trajectories, as well as for future missions that include regolith contact in micro-gravity environments.

Clark et al. (2016) and Bierhaus et al. (2018) collectively describe four campaigns of reduced-gravity TAGSAM collection tests. The "reduced-gravity" tests occurred inside an airplane that flew a specialized parabolic trajectory. During the reduced-acceleration phase of the parabola, the pilots target a specific acceleration; between the various campaigns, the targeted accelerations included 0 g, lunar g, and 0.05 g. The test chambers were vented to the exterior of plane; the typical pre-fire pressure in the chambers was 7.4 psi, which reduces the exit speed of the sample gas relative to vacuum conditions. Fig. 3 shows a series of frame grabs from a 420-fps video acquired during one of the 0.05 g tests; the actual average acceleration during this particular parabola was ~0.03 g. In this test, one edge of TAGSAM contacted the regolith surface first. The sequence shows that the contact of TAGSAM transfers momentum to particles surrounding it — a "billiard ball" effect — kicking some of the particles off the surface. The first row of Fig. 3 captures the moment shortly after first contact of TAGSAM with the surface. Initial ejection of some particles is visible at the lower-left portion of TAGSAM; in subsequent rows, the number of particles expands. In the first and second row, the TAGSAM appears in the differencing because of small yet continued compression into the surface; by the third row, vertical motion of TAGSAM essentially has ended, and most of the visible structure in the differenced image is due to the moving regolith (lower part of the image) and portions of the mechanism that are activating gas release (upper part of the image).

Because the 0.03 g ambient acceleration at the time of test is almost 6000× larger than Bennu's average gravitational acceleration, the distribution of the particles ejected from the surface in this test underestimates the amount and possible velocities of the ejected material. Sanchez et al. (2013) and Ballouz (2017) simulated the contact of TAGSAM-like solid volume with a granular media, and found that particles around TAGSAM are ejected from the surface at speeds up to the contact speed, which for OSIRIS-REx is nominally ~10 cm/s. In addition, low-speed (1–100 cm/s), microgravity impact experiments into simulated asteroid regolith (Colwell, 2003; Colwell et al., 2008; Brisset et al., 2018) demonstrate that ejecta speeds can be comparable to impact speeds.

2.2. Ground testing with low-density material

Implementation and interpretation of TAGSAM testing must consider the environmental differences between a collection test on Earth and the actual sampling event on Bennu's surface. The two most important differences are the relative magnitudes of the gravitational acceleration and the gas pressure of an atmosphere on Earth vs. the vacuum of space for Bennu. The dynamics of the sample gas, and the response of regolith, will be different in Earth-atmospheric and gravity conditions versus those on Bennu. Clark et al. (2016) and Bierhaus et al. (2018) describe the use of vacuum chambers and reduced-gravity aircraft flights to evaluate the collection performance in either low-pressure or lower-surface-acceleration conditions. Bierhaus et al. (2018) also describe a series of tests that use a low-density simulant to mimic the lower weight of particles on Bennu's surface. Although low-density simulants can

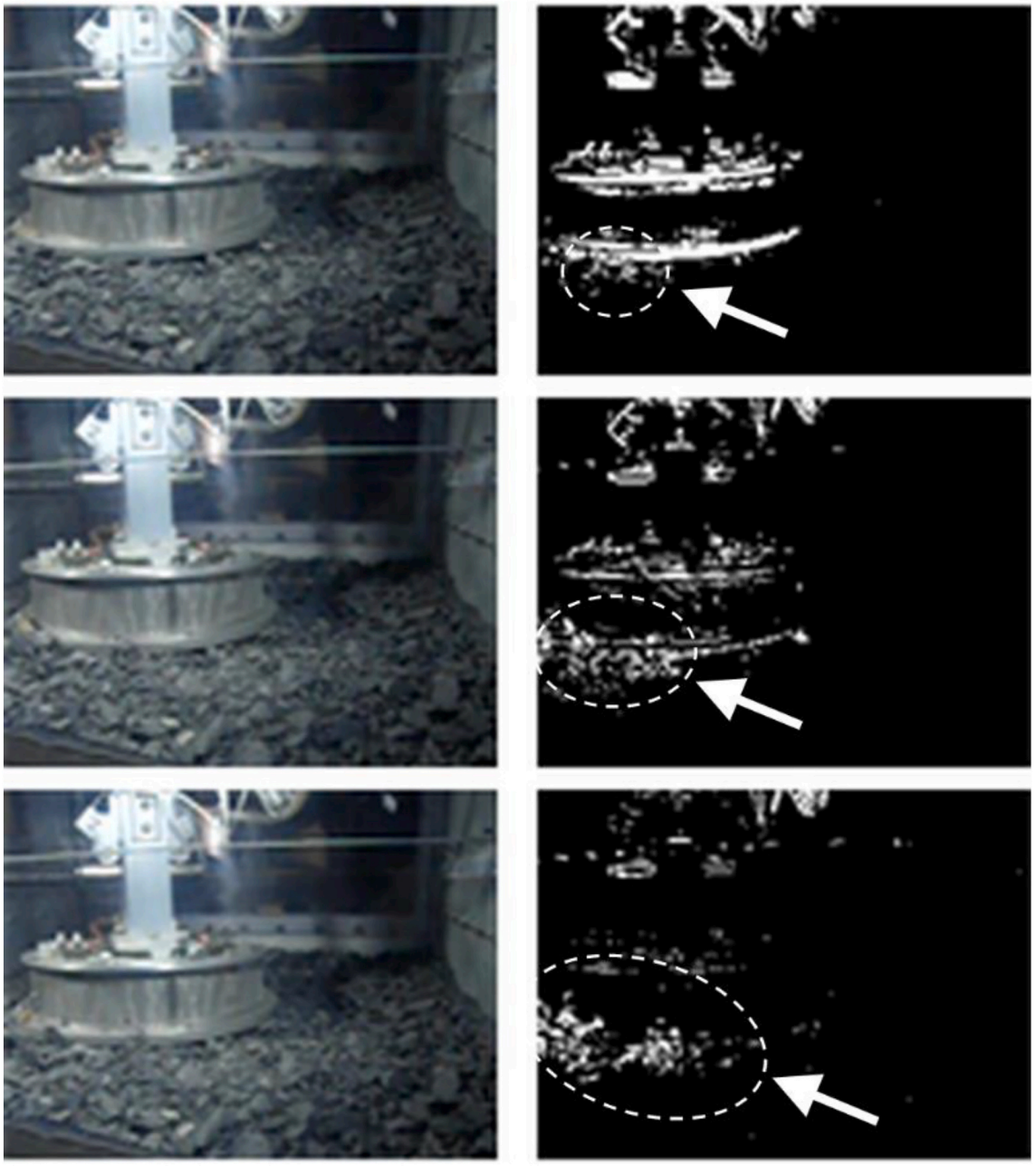

Fig. 3. A series of image exports from a 420-fps video acquired during one of the reduced-gravity test flights (Bierhaus et al., 2018). Time increases from the top row to the bottom row, though the frames are not consecutive. The left column shows three frames from the video. The right column is a binarized version of the difference between the frame shown on the left and the preceding image. The changes in regolith at the lower left of TAGSAM (outlined with dashed ellipses and indicated by white arrows) show that particles are mobilized by the transfer of momentum between the TAGSAM head and the surface particles.

serve as a proxy for lower gravity, they do not match the inertia of material with realistic particle density. However, based on a comparison between realistic-density and low-density tests, Bierhaus et al. (2018) conclude that, below a certain size, the gas drag force on a particle initially exceeds the gravitational force in Earth g (and thus on Bennu). Therefore, low-density simulants are a proxy for particle dynamics on Bennu during the initial phase of gas release. The complete suite of low-density tests included porous polystyrene beads, 2.0-cm-diameter plastic hollow spheres (PHSs), and 2.5-cm-diameter PHSs, with particle densities of 0.02 g/cm^3, 0.31 g/cm^3 and 0.26 g/cm^3, respectively Bierhaus et al. (2018). For the purposes of estimating ejecta speeds and volumes, we used the polystyrene beads, which have the lowest bulk density and thus the lowest weight in Earth gravity. The bead diameters are roughly monomodal, with diameters between 5 and 10 mm (Fig. 4). We used this material to evaluate the range of possible ejection velocities imparted to similarly sized particles on Bennu.

Fig. 5 shows one configuration of the test setup. We filled a wire mesh basket with a single size or mixed sizes of the PHSs and placed the basket with TAGSAM into a vacuum chamber. The wire mesh basket allowed us to use a large volume of simulant in a light-weight container, easily transferred into and out of the vacuum chamber, and provided a low-impedance to the expansion of the TAGSAM gas. We used two sizes of mesh basket: a “small” basket, ~89 cm in diameter and 29.5 cm deep, and a “large” basket, 91.4 cm diameter and 57.8 cm deep. The nearly identical diameter was set by the ability to transfer a filled basket into the test chamber; the difference in height was used to test for depth effects. The pressure inside the chamber prior to each test was 8 to 12 Pa (60 to 90 mTorr). Because we placed the TAGSAM on top of, or in, the

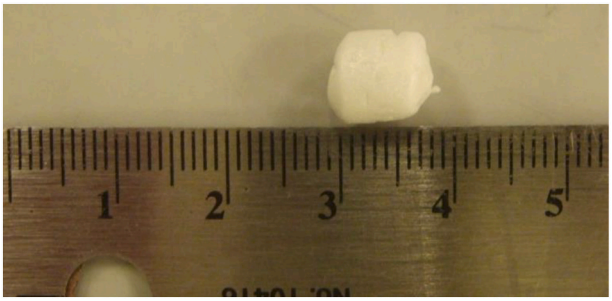

Fig. 4. Dimension of a polystyrene bead. The numbered markings on the ruler are in centimeters; the smaller markings are millimeters.

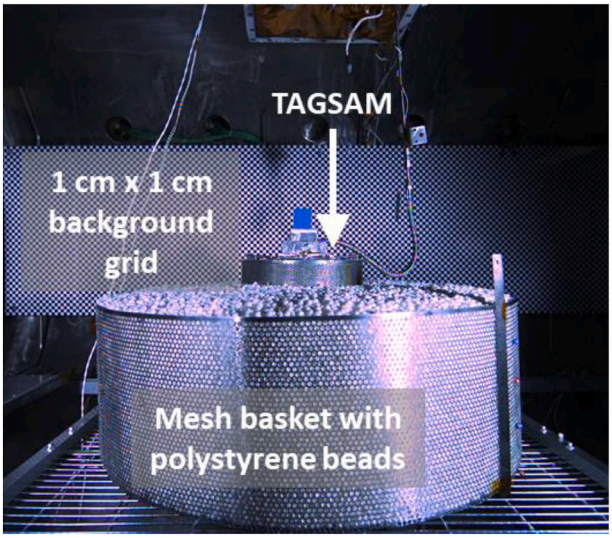

Fig. 5. The small wire mesh basket set up for the low-density simulants. The image shows the basket inside a vacuum chamber prior to a collection test.

regolith simulant, these tests did not capture the transfer of momentum between the TAGSAM and surrounding particles at first contact. The vacuum chamber has viewing ports with glass, through which we recorded and observed the tests. To aid in particle tracking and visibility, we placed a black-and-white grid with 1 cm × 1 cm squares behind the mesh basket (where "behind" is defined by the perspective of the vacuum chamber view port).

Several tests were recorded with a high-quality, 1000–frame per second (fps) Phantom CineMag II video camera, enabling precise timing of dynamics during the test and a more accurate assessment of particle velocities. Because of the single view and camera, full 3D tracking of particles was not possible. However, measurements of dimensions between fiduciaries inside the vacuum chamber, the basket, and TAGSAM enabled an assessment of particle velocities with sufficient accuracy to provide ground-truth for simulations.

Fig. 6 shows several frames from the 1000-fps video taken during one of the polystyrene bead tests. The images show a leading edge of ejected particles leaving the surface at an approximately 45° angle, consistent with the classical primary ejection angle of material ejected due to impact-crater formation Oberbeck (1971); Oberbeck (1975); Cintala et al. (1999); Anderson et al. (2003). The edge of the wire mesh basket introduces an edge effect to material excavation, distorting what is otherwise a clean, expanding inverted cone of material at 45°. As ejection proceeds through a larger volume of material, the ejection speed decreases from that peak value to zero; i.e., material ejected later in the gas release has lower speed than the initially ejected material. Fig. 7 contains some of the same video frames as those shown in Fig. 6, cropped and zoomed to show the expanding ejecta. Four individual points are marked in each frame, and the relative displacement between frames is plotted in the lower right. ("Relative displacement" was measured against the background grid, and the units are in terms of grid elements traveled.) Points are ordered according to proximity to TAGSAM: 1 is the closest, 4 is the most distant. The displacement as a function of time shows that ejection speed decreases as distance from TAGSAM increases. In addition, there is a transition between visibility of discrete particles within the earliest ejecta to a "bulk" flow of later ejecta.

2.3. Mass mobilized by TAGSAM

A parameter of interest is the total mass mobilized by TAGSAM during the sample collection event. For each of the low-density tests, we measured the amount of volume ejected from the wire mesh baskets (see Fig. 8 for a specific example and Table 1 for a summary of the ejected volumes). The tests were designed to evaluate the behavior of ejected material for nominal conditions, as well as "buried TAGSAM" conditions. We evaluated the buried case because uncertainties in Bennu's regolith properties — in conjunction with models that predict regolith dynamics in a microgravity environment (Sanchez et al. 2013), and our testing in reduced gravity (Clark et al., 2016; Bierhaus et al., 2018) — all suggest the possibility that the TAGSAM head could penetrate into the subsurface before the sample gas is released. To evaluate the effect of different TAGSAM depths at the time of gas release, we conducted sample tests with the head at various depths beneath the surface layer of the regolith simulant. Table 1 summarizes the TAGSAM burial depth and corresponding ejected volume. The results indicate that the efficiency of ejecting material increases with the depth of the energy release. This is consistent with experiments done with explosive charges (Nordyke, 1962).

While the wire mesh baskets enable low-impedance expansion of the gas into the vacuum chamber, and thus avoid the severity of unrealistic dynamics to the gas that a solid-walled container would create, they do introduce some degree of potentially unrealistic edge effect to the ejection of material. Based on observations of the ejected material in the high-speed video (e.g., Fig. 6 and Fig. 7), the baskets may reduce the amount of mobilized mass. At later stages in the gas release, the trajectories of mobilized material do not clear the rim of the basket: either the apex of the particle trajectory does not reach high enough, or material ejected near the perimeter hits the side and falls back into the basket. Fig. 8 shows the end state of a test using the polystyrene material with material sloped against the sides of the basket. The symmetric, cylindrical boundary of the basket is an immobile, vertical structure that provides a barrier to escape that would not exist on an asteroid surface. Although buried rocks could mimic such a boundary, the rocks would not form a symmetric, subsurface barrier that prevents the excavation of sub-surface material. Based on the data available, we cannot quantify the degree to which the mesh basket depresses the ejecta volume, but we conclude that the volumes listed in Table 1 are minimum values.

2.4. Ejected material: Crater formation analogy

We can use the test results to evaluate the applicability of the impact-crater analogy for gas release into Bennu. Crater scaling laws use impactor and target parameters to correlate a given-sized impactor with a crater diameter. The scaling laws are an implementation of pi-scaling groups that have been long-used to scale forces (e.g. inertial, gravitational, and pressure forces) relative to each other, see for example Chabai (1977). The TAGSAM gas release results in an extended coupling source region somewhat analogous to a clustered-impact experiment (Schultz and Gault, 1985) where it was shown that standard crater-scaling laws still apply. While more random ejection angles may initially occur, late-stages of excavation evolve into an advancing ejecta curtain with the characteristic angle of 45 degrees. Although there are

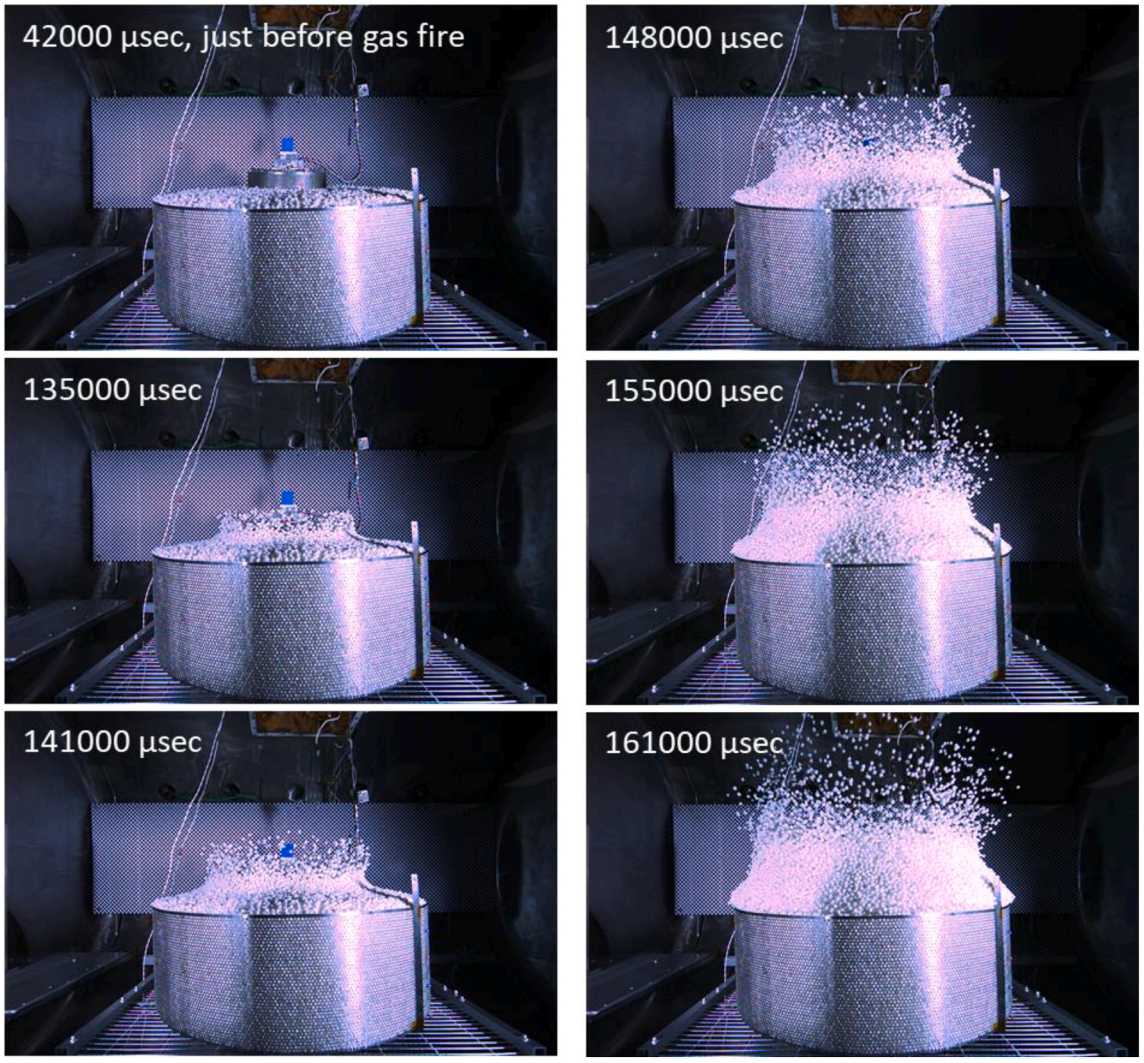

Fig. 6. Time series of a sample collection test with polystyrene beads. Time increases from top to bottom of each column. The expansion of the top layer of particles in a classical cone-shaped ejection pattern is visible. As the expanding surface-excavation wave reaches the edge of the basket, the flowfield becomes distorted by the boundary.

differences between impact cratering and the gas-driven excavation from TAGSAM, we appeal to these proven techniques as a means to bound outcomes from the sampling event. Traditionally, the scaling laws address two end-member regimes: (1) the strength regime, where the target strength halts crater growth, and (2) the gravity regime, where the target gravity halts crater growth (see Holsapple, 1993 for a review on scaling laws and the two regimes of crater growth). On larger planetary surfaces (terrestrial planets, large and mid-sized moons), small craters form in the strength regime and large craters form in the gravity regime, where "small" and "large" are target-dependent. In the case of a potentially low- or no-strength rubble-pile asteroid with microgravity, like Bennu, it is difficult to know a priori where the strength- and gravity-controlled crater regimes exist, although the Hayabusa2 impact experiment provides evidence that rubble-pile carbonaceous asteroids have low strength (Yuichi et al., 2020). Although the surface gravity is small, the effective target strength could also be small; an additional complicating factor is that as crater size decreases, the details of any individual crater's formation become sensitive to the pre-existing boulder population on the surface (Tatsumi and Sugita, 2018). We evaluate both a strength-controlled and gravity-controlled TAG event.

For a strength-controlled crater, the crater radius R_s is (Housen and Holsapple, 2011):

$$R_s = \left(\frac{\rho}{m_i}\right)^{-1/3} H_2 \left(\frac{\rho}{\delta}\right)^{(1-3\nu)/3} \left(\frac{Y}{\rho\, v_i^2}\right)^{-\mu/2} \quad (1)$$

where δ is the impactor density, m_i is the impactor mass, ρ is the target density, Y is the target strength, and H_2, ν, and μ are constants. For a gravity-controlled crater, the crater radius R_g is (Housen and Holsapple, 2011):

$$R_g = \left(\frac{\rho}{m_i}\right)^{-\frac{1}{3}} H_1 \left(\frac{\rho}{\delta}\right)^{\frac{2+\mu-6\nu}{3(2+\mu)}} \left(\frac{g\, a}{v_i^2}\right)^{-\frac{\mu}{2+\mu}} \quad (2)$$

where a is the impactor radius, H_1 is a constant, and all other variables are as given in the strength-controlled case. In both the strength and gravity regimes, the corresponding crater mass M is:

$$M = k_{crater}\, \rho R^3 \quad (3)$$

where k_{crater} is a constant dependent on material properties. Housen and Holsapple (2011) indicate that k_{crater} is 0.75 for cohesive soils (perlite/sand mixture) and 0.4 for dry sand; we use those values for the strength and gravity-regime calculations, respectively. Table 2 lists the other target values used from Housen and Holsapple (2011). The differences between Bennu's surface and sand or perlite add uncertainty to our derived values of mobilized mass. Because we include both gravity-

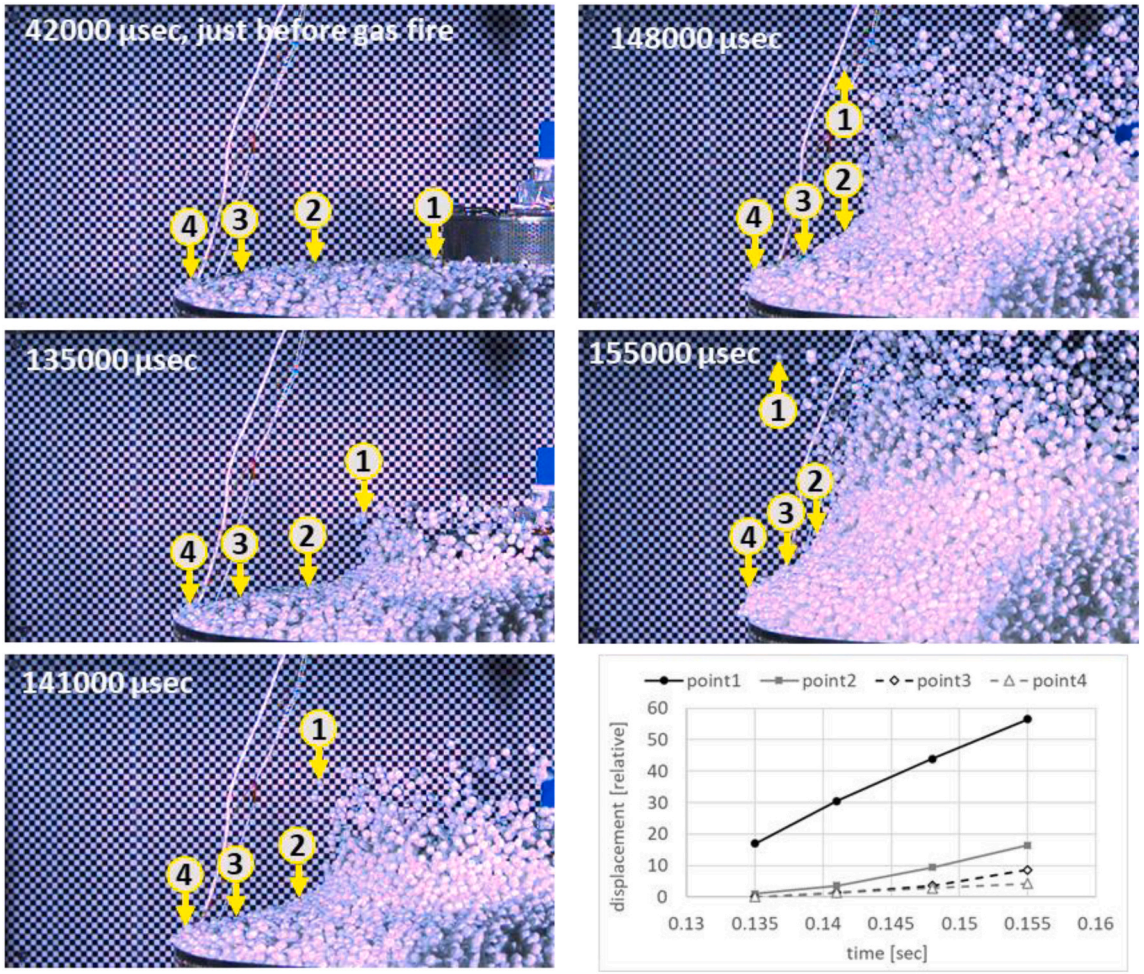

Fig. 7. Some of the same video frames from Fig. 6, zoomed and cropped to illustrate the expansion of ejected material. Points 1 to 4 are tracked between frames, and their relative position in the 2D plane of the camera is plotted in the lower right. The displacement and relative amount of material mobilized as a function of time demonstrates an inverse mass–ejection speed relationship, i.e. more mass is ejected at lower speeds.

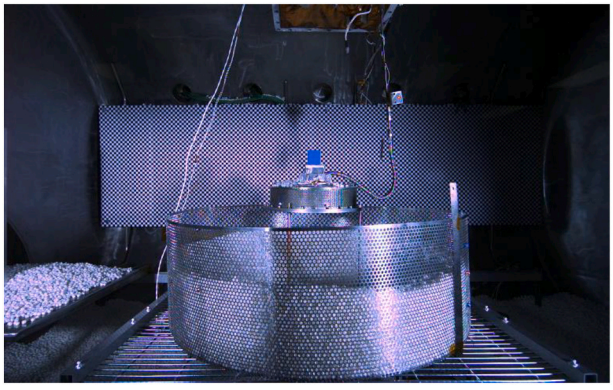

Fig. 8. TAGSAM collection test #5 (Table 1) using low-density material. The picture shows the state after the gas was fully expended. In this test, TAGSAM ejected about 0.12 m^3 of material.

and strength-controlled derivations and a range of material strengths, we expect that the range of excavation masses that we find also accounts for differences between the analogous material properties that we assumed and actual Bennu values. We used a density of $\rho = 1190$ kg/m^3 (Lauretta et al., 2019a).

Creating an analogous material for the impactor is more challenging. On the one hand, the timescale of the gas release (of order 5 s) is slower

Table 1
Measured volume and maximum speeds of ejected material from low-density testing. The corresponding mass at Bennu assumes a 1200 kg/m^3 bulk density (Scheeres et al., 2019). Tests #1 and #6 are not listed: test #1 was a check-out run without material, and test #6 was run at ambient pressure; thus, the results are not applicable to Bennu.

Test #	Volume ejected [m^3]	Mass at Bennu [kg]	v_{ej}, max obs. [m/s]	v_{ej}, max est. [m/s]	Notes
2	0.158	190	8	11.3	Large basket; head buried to ~0.19 m
3	0.158	190	6	8.5	Large basket; head buried to ~0.16 m
4	0.175	210	6	8.5	Large basket; head buried to ~0.5 m
5	0.120	144	6	8.5	Short basket; head restricted to remain on original plane of simulant
7	0.213	255	10	14.1	Large basket; head allowed to sink to equilibrium depth simulant pre-gas fire, about 7.5 cm

Table 2
Crater scaling law parameters used to estimate the total mass ejected by the TAG event for the target, Bennu. Values are from Housen and Holsapple (2011). We use the sand values for the gravity-regime calculations and the perlite/sand mixture values for the strength-regime calculations. A dash indicates that the value is not given in the source reference.

Parameter	Sand value	Perlite/sand mixture
μ	0.41	0.35
ν	0.4	0.4
C_1	0.55	0.6
H_1	0.59	–
H_2	–	0.81
k_{crater}	0.4	0.75

than typical timescales associated with impacts (approximated by the very short time it takes the impactor to travel its diameter). On the other hand, the propagation of the gas through the regolith likely occurs at hypervelocity speeds for much or all of its expansion. The initial peak speed of the gas while exiting TAGSAM is around 800 m/s. Because the porosity in Bennu's regolith is occupied by a vacuum rather than an atmosphere, the expansion of the gas through the interstitial spaces of the regolith will be a choked flow. In the case of choked flow, the expansion speed of the gas is its sound speed, which depends on gas temperature. Specifically, the sound speed v_g of a gas is

$$v_g = \sqrt{\frac{\gamma R T}{m_{mol}}} \tag{4}$$

where γ is the adiabatic constant (the ratio of the specific heat at constant pressure to the specific heat at constant volume), R is the universal gas constant, T is the temperature, and m_{mol} is the molecular mass of the gas. The majority of the gas is nitrogen (the remainder is a small amount of helium). We know γ, R, and m_{mol}; the remaining parameter to determine is the temperature. The TAGSAM gas reaches equilibrium with the environment as it expands unto the subsurface. Thus, the temperature of the gas is controlled by the ambient temperature. Fig. 9a plots the temperature profile with depth for the primary TAG site, Nightingale (at approximately 56°N, 42°E, see Section 4.1), for the date and time of the sampling event (October 20, 2020 at ~3 pm local solar time); see DellaGiustina et al. (2019) and Rozitis et al. (2020) for details on the model development. The depth covers about 8 skin depths, or 16 cm for a 2 cm skin depth. (A thermal skin depth is the depth at which the thermal wave reduces by $1/e$). Below this depth, the seasonal effects are a greater influence on the temperature. For the depths relevant to mass mobilization, we can consider the minimum value (~250 K) in this plot as the lowest temperature that the gas will experience in the subsurface when excavating material. Fig. 9b plots v_g for the range of temperatures given in the 8-skin-depth profile; the minimum value across this temperature range is ~319 m/s. Table 3 lists the other values used for the gas-based impactor model. The speed and density values are the values for the gas as released underneath TAGSAM, as these are the most relevant for regolith mobilization.

Table 3
Impactor parameters used to estimate the mass-velocity distribution of material ejected during the sampling event.

Symbol	Description	Value	Unit
m	impactor mass	0.061	Kg
U	impactor speed	325–800	m/s
δ	impactor density	0.036	kg/m^3
γ	ratio of specific heats	1.4	–
R	gas constant	8.314	J/(mol K)
m_{mol}	molecular weight of gas	28.014	g/mol

For leading-edge gas propagation through Bennu's subsurface to be at hypervelocity, the sound speed through Bennu's regolith must be lower than the gas velocities shown in Fig. 9b. Observations of Bennu's bulk density, shape, and surface regolith indicate that it is a rubble pile with total porosity between 50 and 60% (Barnouin et al., 2019). Although we do not have direct measurements of Bennu's subsurface sound speed, we can reference known values from other porous, granular materials. In general, such materials have low sound speeds. Oelze et al. (2002) investigated sound speed in a variety of granular material types (clay, silt, sand, and organic matter) and find speeds between 86 m/s to 260 m/s; Cooper et al. (1974) report sound speed velocities in the upper meters of the lunar regolith to be 100 m/s; Teramoto and Yano (2005) measure the speed of sound through granular materials of uniform and mixed sizes (40 μm to 220 μm) and find speeds between 92 m/s and 171 m/s. Thus, it is a reasonable assumption that the nitrogen gas front will propagate through Bennu's subsurface faster than the sound speed of the Bennu regolith. The speed of gas behind the front will be lower; how much lower will depend on the porosity. The details of the bulk gas expansion differ from the rarefaction wave that drives excavation during an impact, a difference that remains a limitation of the impact-scaling analogy to gas-driven excavation. Nevertheless, the crater-based excavation results provide a baseline comparison for what will occur during the sample collection.

Fig. 10 plots the ejected mass for both the strength and gravity regimes. Because Bennu's bulk target strength is low (as a rubble pile) but unknown quantitatively, we plot the mass for strengths between 1 and 100 Pa. We choose this range to include the estimated Ryugu cratering strength of <1.3 Pa (Arakawa et al., 2020), and two orders of magnitude larger, which should be a reasonable range of possible values for Bennu. (However, individual boulders on Bennu's surface may have strength within the range of terrestrial rock; Ballouz et al. (2020). In the gravity regime, the speed of the nitrogen gas through the regolith spans from the peak speed of release from TAGSAM, ~800 m/s, to the "steady state" expansion of the gas through the subsurface, around 325 m/s for 255 K. The full range of ejected mass spans 12 kg (lowest strength-regime value) to 165 kg (highest gravity-regime value).

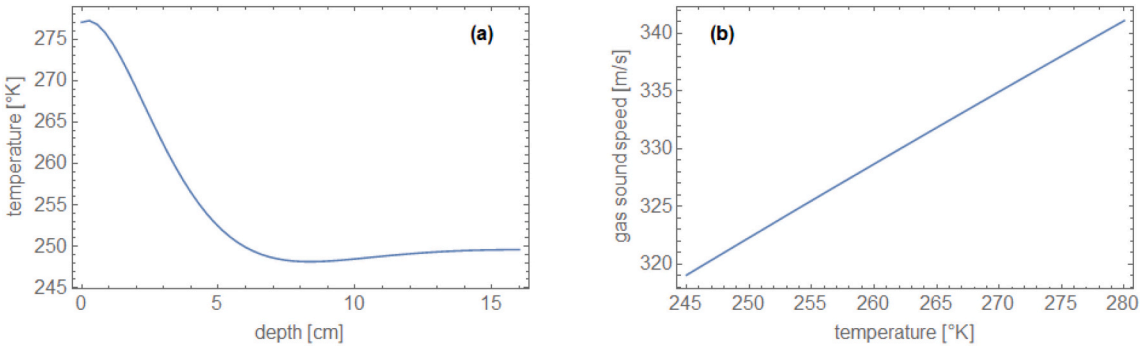

Fig. 9. (a) Temperature as a function of depth at the Nightingale TAG site (approximately 56°N, 42°E) at the time and date of TAG: October 20, 2020 at a local solar time of ~3 pm. (b) Nitrogen gas speed as a function of the temperature range in the near subsurface of Nightingale at the time of TAG specified in panel (a).

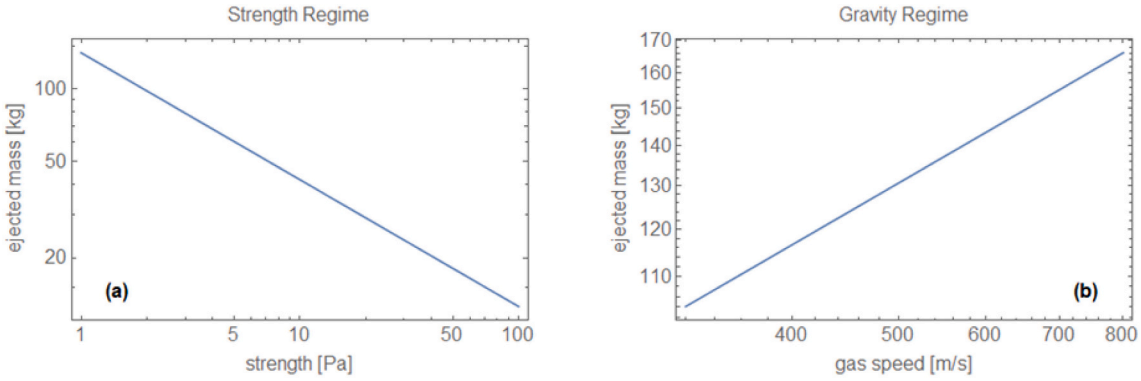

Fig. 10. Mass ejected by the TAG event. (a) Range of possible masses in the strength regime given different effective strengths for Bennu. (b) Range of possible masses in the gravity regime given a range of gas speeds.

Testing with low-density simulants demonstrated that the generation of ejecta by TAGSAM shares similarities with the processes that drive crater ejecta. Energy is deposited into a small volume in a short amount of time, creating pressure differentials that expand in a roughly hemispherical manner. Fig. 11 shows the ejecta points identified in Fig. 7 with a line that represents an idealized 45° trajectory. The leading-edge of the ejecta leave the surface at a ~ 45° angle, which also happens to be the classical angle for crater ejecta during the bulk excavation flow (Oberbeck, 1971; Oberbeck, 1975; Cintala et al., 1999; Anderson et al., 2003). Inspection of the ejecta in Fig. 6 and Fig. 7 shows a gradient in population density between the earliest ejected material and that ejected later. This indicates an inverse mass–velocity magnitude relationship: a small amount of mass leaves at the highest possible ejection speeds, and decreasing ejection speeds correspond to increasing amounts of ejected mass. The finite diameter of the wire mesh basket prohibits full evaluation of the ejection dynamics throughout the entire ejection phase, the results described here apply to the early ejecta. To ensure our simulations capture the range of possible ejection angles, our simulations include ejection angles from 0°-90° (Section 3.2). Although some details differ between an impact cratering event and injection of the sample gas, the similarity in ejecta behavior motivated a crater-ejecta formulation for defining the mass–velocity magnitude relationship for material ejected by TAGSAM.

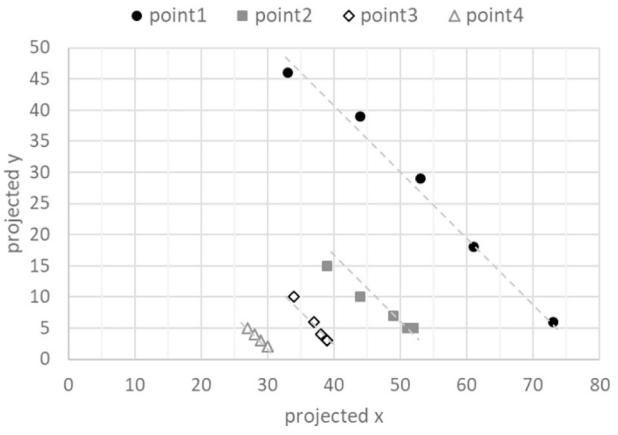

Fig. 11. The points identified in Fig. 7, plotted in projected (x,y) space. The coordinate system is defined by the lower left of the black and white grid seen in Fig. 6 and Fig. 7. Five time steps are shown for each particle, with increasing time corresponding to decreasing x-values and increasing y-values. The dashed gray line through each set of points is an idealized 45° trajectory. Though there is minor variation, each of these ejected particles approximately follows the 45° trajectory.

2.5. RegoSim and predicted initial conditions

RegoSim ("Regolith Simulation") is the software tool developed at Lockheed Martin to simulate trajectories of regolith particles entrained in the TAGASAM gas flow. These trajectories are specifically for particles mobilized and launched away from the asteroid surface; RegoSim does not predict the volume of regolith disturbed by the TAG event. RegoSim spawns regolith into the gas flow field with user-defined constraints for initial position, initial velocity, particle size/mass distribution, particle drag coefficient, and time relative to TAGSAM firing, which accounts for the blowdown of gas dynamics after initial gas release. Particle-spawning parameters are randomized, and the total number of particles is user-specified. This constitutes a Monte Carlo simulation of particle trajectories with results suitable for statistical analysis. Each particle trajectory is integrated separately through the gas flow field. Particle-particle interaction is not considered in the present version of the software, and localized influences of particles on the gas flow field are also neglected. These are reasonable assumptions outside the TAGSAM head, given that the essentially radial expansion of gas into the hemispherical volume above TAGSAM quickly ejects particles from a dense configuration to a disperse configuration. (Fig. 7 demonstrates the rapid separation of the earliest particles, and Fig. 11 demonstrates that even later, slower moving ejecta follows a 45° trajectory.) The TAGSAM effluent gas flow is supplied to the RegoSim via a mesh with embedded gas properties.

Data generated by RegoSim provided a means to estimate the maximum possible ejection speeds as a function of particle diameter. Fig. 12 plots the ejection speed as a function of diameter for the

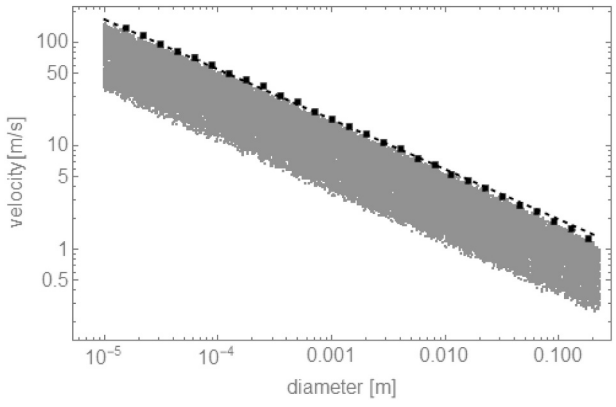

Fig. 12. Particle speeds estimated by RegoSim (gray points), with maximum (small black squares) values in discrete diameter bins, and a best-fit power law to the maximum (black dashed line) data. The best fit makes it possible to predict maximum ejection speed as a function of particle diameter.

simulated particles. At any given diameter, there are a range of possible speeds, due to the decay of gas pressure over time. In reality, any speed between the maximum shown and 0 m/s is possible, depending on the time at which the particle is ejected during the gas release. The band of velocities shown for a given particle diameter in Fig. 12 is due to the modeling of the earliest phases of gas release to capture the maximum possible speeds. The best fit to the maximum speeds are $v_{ej} = 0.64\ d^{-0.48}$, where d is particle diameter in meters and v_{ej} is in meters per second.

Bart and Melosh (2010) measured boulder diameters and distances from source craters to derive ejection velocities and fits to $d_{max} = a\ v^b$, where d_{max} is the largest boulder at ejection speed v, and a and b are fits to their data. They find that b ranges from −0.5 to −3.7 (see their Table 3 and Fig. 13). The variation in b is correlated with source-crater diameter (see also Vickery, 1986); larger craters have increasingly negative b. In other words, as ejection speed increases, the maximum boulder size decreases. The similarity between our value and the minimum value found by Bart and Melosh, 2010 for the smallest craters ($b \sim -0.5$. in both cases) is intriguing and worth future investigation. Because of the substantial differences in scale (the minimum crater diameter that Bart and Melosh (2010) examined is ~200 m), regolith properties, particle sizes, and ejection mechanisms, it is premature to link these values from TAGSAM and crater ejecta. Indeed, Schultz (1992) does not find evidence of size sorting for ejecta particles with sizes of 1 mm and 0.5 μm.

2.6. Correlation between tests and simulations

Our simulations predict both the amount of ejected mass (Fig. 10) and speed of ejected material (Fig. 12). We can compare these values with data from empirical testing to evaluate the ability of the simulations to predict values not captured in the test data.

We evaluate the relative accuracy of the crater-based analogy by comparing test results of ejected volume with predictions from the scaling laws. The low-density test material was a strengthless, granular material (polystyrene beads). We estimate the gravity-controlled ejected mass for the test material in Earth conditions using the parameters for sand in Table 2, and Earth's gravity in place of Bennu's gravity. This results in 0.43 kg of ejected mass. The bulk density of the material is 5.9 kg/m^3, thus the ejected mass corresponds to 0.07 m^3 of material. Comparing this value to the result from test #5 (the most analogous condition to the Bennu calculations above), 0.12 m^3, the crater-based analogy simultaneously achieves a useful level of accuracy — 42% discrepancy is reasonable considering the number of caveats when applying the crater analogy to the TAGSAM gas release — and is an underestimate of the actual test data. Thus, the TAG event could mobilize more than the 165 kg maximum mass (Fig. 10).

For 1-cm-diameter particles, the approximate size of the polystyrene material, the RegoSim predicted maximum ejected speed is 5.8 m/s (Fig. 12). The high-speed video of the tests enabled us to estimate the vertical component of the ejected material. Given an ejection angle of 45° (Fig. 11), we translate the observed vertical speed to a total speed by

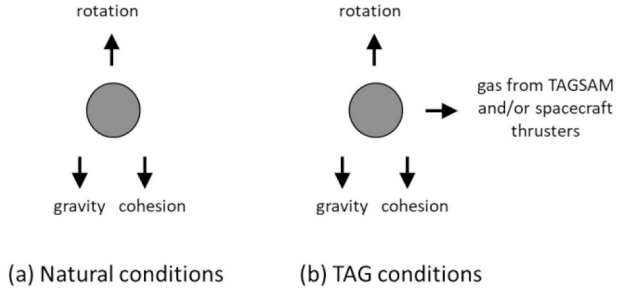

Fig. 13. Dynamics affecting particle motion (a) under natural conditions and (b) during TAG conditions. The arrows are meant to indicate general direction and do not reflect relative magnitudes.

$v_{ej}(tot) = v_v(obs)/\cos 45°$, where v_{ej}(tot) is the total ejection speed and v_v(obs) is the observed vertical speed. Table 3 lists the observed vertical component of the ejection speed and an estimated total speed. Test #5 is most analogous to the RegoSim analysis (the TAGSAM head is not buried in the subsurface at the time of gas release), and the observed ejection speed, adjusted for projection effects, is 8.5 m/s, or about 47% larger than RegoSim. For the purposes of correlating the RegoSim results, this comparison is sufficient; i.e., we determined that material can be ejected at speeds well above Bennu's escape speed, and thus TAGSAM will eject material into all three velocity-magnitude regimes of interest (Fig. 2).

2.7. Particle mobility beyond the immediate TAG site

The TAGSAM sample gas, at first localized underneath the TAGSAM head, expands radially into the surrounding vacuum. Some of the gas penetrates into the subsurface and contributes to material mobilization, as described previously. Some of the gas expands radially away from the surface, having less interaction with regolith. The radial direction parallel to the surface has a scouring effect on surface particles, potentially like wind blowing across granular material. Here we describe a simple estimate of a 1D force balance in the radial direction for a particle on Bennu, which follows formulations from those in Scheeres et al. (2010) and Hartzell and Scheeres (2011). This analysis describes the potential behavior of particles that "roll" across the surface, rather than being ejected onto a trajectory (Section 3 describes particle trajectory integrations). Such rolling, or lateral translation, away from the TAG location is expected for some Bennu regolith particles, without ejection except perhaps for transient hops. A comprehensive treatment of 3D accelerations would include tangential components of the cohesion and variation in acceleration from the gas due to particles shadowing each other, among other factors. A detailed acceleration model of particles on Bennu's surface may be possible after sample collection, given the expected resolution of the data that will be acquired during TAG (Lauretta et al., 2017). We use the simplified model to reduce the number of assumptions, and thus the potential for systematic biases in the result if those assumptions are incorrect. Data acquired during the TAG event may determine whether this simple, 1D model is sufficient or if more sophisticated treatment is needed.

Under normal conditions, a particle on Bennu's surface is held in place by a combination of gravity and cohesion. Centripetal acceleration, due to rotation, acts in the opposite direction; because this term depends on the speed of the rotating surface, it is a function of latitude. First we consider gravity and rotation (Scheeres et al., 2010), which here we call the modified acceleration due to gravity, or a_{mg}:

$$a_{mg} = \left(\omega^2 cos^2\Delta - \frac{4\pi G\rho_b}{3}\right) R_a \tag{5}$$

where ω is the asteroid angular rate, G is the gravitational constant, Δ is the latitude of the particle, ρ_b is the asteroid bulk density, and R_a is the asteroid radius. The first term is from rotation, the second term is from gravity. Next we consider the cohesion force F_c, which is approximated by $F_C = 3.6 \times 10^{-2} S^2 x$, where S is a cleanliness factor between 0 and 1, and x is the particle radius Scheeres et al. (2010). Setting $F_C = ma_C = 3.6 \times 10^{-2} S^2 x$, defining $m = \rho_p 4\pi x^3/3$ (where ρ_p is the particle density), then solving for a_c gives:

$$a_c = \frac{3}{4}\frac{3.6\times10^{-2}}{\rho_p \pi}\frac{S^2}{x^2} \tag{6}$$

The total acceleration on a particle is thus

$$a_T = a_{mg} + a_C = \left(\omega^2 cos^2\Delta - \frac{4\pi G\rho_b}{3}\right) R_a - \frac{3}{4}\frac{3.6\times10^{-2}}{\rho_p \pi}\frac{S^2}{x^2} \tag{7}$$

where the negative signs indicate the direction is towards the surface. During TAG, this condition is revised to include a term from the gas expansion from TAGSAM. Fig. 13 illustrates the free-body diagram of

these cases.

The mobility of a particle in response to gases from TAGSAM are more naturally considered in terms of pressure. Assuming spherical particles with half of the particle acting as the active area for an equivalent force, Fig. 14 plots the pressure for gravity and cohesion as a function of particle size for the high- and low-latitude TAG sites. At diameters less than tens of centimeters, cohesion dominates, and because cohesion is independent of latitude, the two curves are the same. At large particle diameters, gravity dominates, and here the two curves diverge due to their different latitudes, and thus different a_{mg}. In each case, there is a minimum pressure, which corresponds to the particle diameter that is mobilized most easily. This is similar to wind-driven particle motion on Earth; for example, see Kok et al. (2012) and Greeley and Iversen (1985). However, the preferred particle size varies: on Earth and Mars, this particle size can be of order 100 μm, while on Bennu, it is tens of centimeters. At small diameters, cohesion dominates; at large diameters, gravity dominates. There is a minimum in the combined pressure, at roughly 56 cm for the high-latitude site and roughly 75 cm for the equatorial site, where the two forces contribute equally. The minimum is different between the two sites because of their different latitudes.

Another consequence of a minimum at this particle size is the nature of particle migration across Bennu's surface in response to input energy — be it from impact, YORP (Yarkovsky–O'Keefe–Radzievskii–Paddack) spin-up, or something else. Because the predicted minimum occurs at diameters near 0.6 m, the inertia at this size is more than 10^5 that of a 1-cm-diameter particle. A force that is sufficient to mobilize a 0.6-m particle, but not smaller particles, will result in a low acceleration of the particle. A force that is sufficient to mobilize a broader range of particle sizes will result in a distribution of accelerations, with the smaller particles receiving higher accelerations, with greater likelihood of achieving speeds that lead to escape. This process could explain, at least in part, the preferential loss of smaller particles on the surface. Although the smaller particles are harder to mobilize because of cohesion, if they are mobilized, the acceleration needed to do so leads to speeds that result in escape.

By observing which surface features are mobilized during TAG, as a function of distance from the TAG site (which provides information on the magnitude of the pressure from the spacecraft gases) and particle size, we can derive information on the cohesive forces for particles on Bennu.

3. Particle dynamics simulations

The RegoSim and laboratory testing establish a basis for defining the initial conditions of ejected particles. Determining the fate of these ejected particles requires integration of those trajectories around Bennu. Because of the surface acceleration variation across Bennu's surface (Scheeres et al., 2010; Scheeres et al., 2019) as a function of latitude, we took two approaches to simulating the particle dynamics. First, we ran a set of particle trajectory simulations that launched particles from a range of surface positions spanning the likely latitude range of the TAG sample site (between −65° and + 65° latitude; because we are using a spherical Bennu, the results for the northern and southern hemispheres are symmetrical, and thus we use ejection locations between 0°N and 65°N latitude). The ejection velocities covered the range of predicted ejection speeds and angles: particles were ejected from the surface at speeds of 1 cm/s to ~9 m/s, angles of 0° to 90° from local vertical, and azimuths between 0° and 360°. These simulations informed the sensitivity of particle fate from launch location and launch velocity. Second, we ran more detailed simulations for two specific, hypothetical TAG locations, one at high latitude (65°N) and one at low latitude (0°N, i.e. at the equator); the ejection-speed range in these simulations was restricted to values that resulted in either re-impact with Bennu to slightly above escape speed. We restricted the ejection speed of these simulations to explore more specifically the dynamics of particles that remain near Bennu; such particles are of most interest relative to continued interaction with Bennu and subsequent spacecraft operations. Compared with the simulations that include ejections from a broad range of latitudes, these simulations provided a higher-fidelity description of what to expect at a given TAG location. We discuss a comparison of these hypothetical sites with the OSIRIS-REx mission's actual primary and backup TAG sites in Section 4.1.

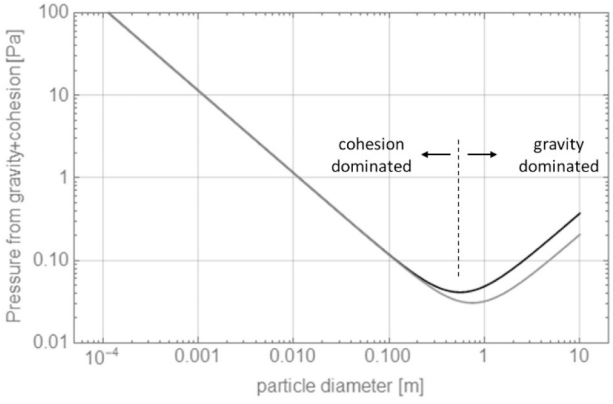

Fig. 14. Pressure on particles resting on Bennu's surface for a 65° N latitude TAG site (black line) and an equatorial TAG site (gray line). The minimum in the curves corresponds to the particle sizes that are the easiest to move.

3.1. Dynamical model description

The two types of trajectory calculations used common simulation capabilities and parameters. The orbit integration uses a 6th-order Runge-Kutta engine, with Bennu's central-body gravity and J2 term. The non-gravitational force model includes SRP and shadowing by Bennu. Orbit propagation continues until a particle reaches one of three fates: (1) re-impact with Bennu, (2) the particle passes beyond Bennu's Hill Sphere and is considered escaped into an independent heliocentric orbit, or (3) the end of the maximum integration time, 21 days. The 21-day integration corresponds to ~5% of Bennu's heliocentric orbit, and thus, as a simplification for the analysis, we assumed a fixed solar distance at 1 AU. The change in SRP over the full 21 days is ≤13%, and over the few-day lifetime of most particles (see later discussion in this section) is only a few percent. For a discussion of long-term evolution of particles orbiting Bennu, see McMahon et al. (2020). For all particles, we recorded the position and velocity relative to Bennu at the end of its integration time.

Chesley et al. (2020) and McMahon et al. (2020) examine the dynamics of naturally ejected particles from Bennu. They use acceleration models that include several factors we do not consider here, such as the effect of infrared emission and reflected sunlight from Bennu. Such accuracy is necessary to match the dynamics of the observed particles. Our intent here is to describe the broad ensemble behavior of thousands of discrete particles ejected by the TAG event. Our acceleration model accounts for ~98% of the accelerations described in Chesley et al., 2020; see their Table 1). Thus, while our acceleration model does not account for all the factors that affect particle dynamics, the general outcomes are robust.

Table 4 lists the Bennu properties used for the integrations. The first round of these analyses was completed during the OSIRIS-REx development phase (calendar year 2013) and used the best information available at that time. Since that initial analysis, we have rerun the simulations using updated values derived from measurements made during mission operations. The results we report in this paper utilize the updated Bennu parameter values.

The initial simulations were performed in 2013 and 2014, at which time the OSIRIS-REx team used a radar shape model, described by Nolan

Table 4
Bennu properties used for the trajectory simulations. Initial simulations were done during the development phase of OSIRIS-REx, prior to the availability of more accurate values determined during the operational phase of the mission. The simulations here use the updated values for these parameters, as reported in Lauretta and DellaGiustina et al. (2019).

Bennu property	Unit	Value
Mean radius	M	245
Bulk density	kg/m^3	1190
Mass	Kg	7.329×10^{10}
Average albedo	–	0.044
Rotation period	Hrs	4.296
Particle density	kg/m^3	1800
J2	–	0.0192
P_0 (solar flux)	kg km^3 / s^2 / m^2	108

et al. (2013). The shape model was of sufficient fidelity to show Bennu's top-like shape. Though not spherical, the shape is more regular than those of other small asteroids (e.g., Itokawa), and thus we used a spherical central body for Bennu. Although this choice introduces some differences when integrating versus using an actual shape model — due to the gravitational acceleration term and tracking impact locations — the overall conclusions for broad aspects of particle dynamical behavior remain appropriate.

The SRP model used is

$$a_{SRP} = \frac{(1+\propto) P_0}{B\, d^2} \tag{8}$$

where a_{SRP} is the magnitude of the SRP, α is the particle albedo, P_0 is the solar flux, B is the mass-to-area ratio of a particle, and d is the Bennu-Sun distance. We used a simple conical shadowing model to determine the extent of Bennu's shadow. SRP was set to zero any time a particle's position placed it inside the shadow.

3.2. Simulations with a broad sweep through parameter space

The first set of particle-trajectory simulations is a pair with common input parameters except for ejection speed. Parameters in the generation of the particles included ejection latitude, longitude and particle size. Particle sizes of interest spanned from 1 mm (a little smaller than the few-millimeter-diameter minimum size for which potential particle abundances existed, based on observations of Itokawa (Tancredi et al., 2015) and interpretations of Bennu's thermal inertia (Emery et al., 2014), to 30 cm (larger than the mission requirement to detect a 10-cm-diameter satellite, to ensure sufficient statistics at 10 cm).

Within the first set of simulations, the velocity-magnitude regime used differs. The first simulation modeled 10,000 particles and spanned the full range of possible ejection speeds, which include values well above Bennu's classical escape speed of ~0.2 m/s. The high end of possible ejection speeds (Sections 2.5 and 2.6) readily remove particles from the system. However, including this complete velocity-magnitude range in the first set of simulations ensured that we captured the full range of dynamical behavior dependent upon ejection speed. The results of the first simulation allowed us to target a more specific ejection speed range to explore the complex behavior for particles ejected near v_{esc}. The second simulation of this pair included ejection speeds between 0.1 and 0.3 m/s. Table 5 lists the input values used for both sets of simulations. Fig. 15 plots the available starting locations of all ejected particles from these simulations; the locations fall along a great circle that connects the two (lat, lon) pairs of (0°, 65°) and (65°, 0°).

We generated particle diameters by selecting from a uniform random distribution between 1 mm and 30 cm. Once a particle received a diameter, we assigned a total body-fixed ejection velocity by randomly selecting a value between 1 cm/s and the maximum possible speed defined by the fit to the RegoSim data set, and randomly selecting values for ejection elevation and azimuthal angles.

Table 5
Summary of the range of input values for particle trajectory simulations. The first simulation examined the complete range of expected ejection velocities predicted from the best-fit function of the RegoSim results (Fig. 12). Based on the results of the first set of simulations, we ran a second simulation that restricted the maximum ejection speed to 0.3 m/s, which focuses on particles that either re-impact Bennu or remain within the Hill Sphere for the duration of the 21-day integration.

Parameter	Unit	Minimum value	Maximum value
Body-fixed ejection speed, 1st simulation	m/s	0.1	9.1
Body-fixed ejection speed, 2nd simulation	m/s	0.1	0.3
Particle diameter	m	0.001	0.3
Ejection azimuth (relative to north)	deg	0	360
Ejection angle from local vertical	deg	0	90
East longitude[1]	deg	0	65
Latitude[1]	deg	0	65

[1] Longitude and latitude were parameterized to fall on a great circle that connects the two points (lat1, lon1) = (0°, 65°) and (lat2, lon2) = (65°, 0°). See text for details.

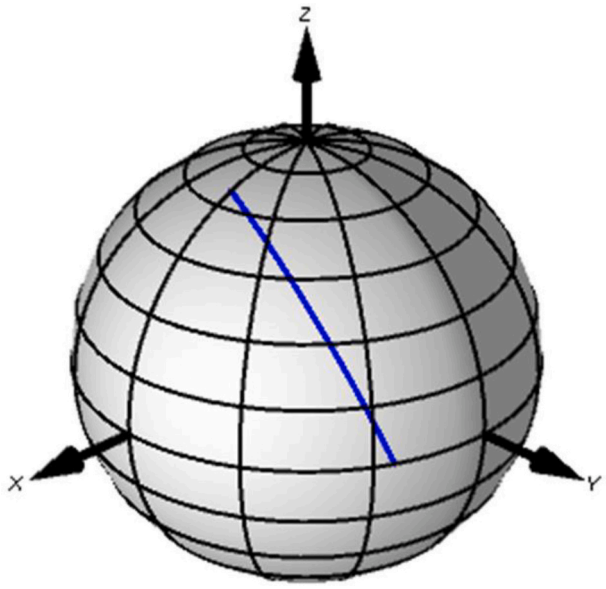

Fig. 15. The blue line, connecting 0° lat, 65° lon to 65° lat, 0° lon, indicates the originating locations of particles in the first set of simulations. Latitude lines are plotted every 15°, and longitude lines are plotted every 30°. (For interpretation of the references to colour in this figure legend, the reader is referred to the web version of this article.)

Fig. 16 plots particle lifetime vs. body-fixed ejection speeds for the 10,000-particle simulation that spans the full range of ejection velocities. The left panel plots the full ejection-velocity range of the simulation. The data fall into three general categories: (1) particles moving slowly enough ($v_{ej} < v_{esc}$) that they travel on suborbital trajectories and re-impact Bennu; (2) a regime ($v_{ej} \sim v_{esc}$) in which a particle could re-impact Bennu, remain in orbit for the duration of the integration period, or escape; and (3) particles moving fast enough ($v_{ej} > v_{esc}$) that they directly escape. To emphasize the transition between the three regimes, the right panel plots the same data, restricted to ejection speeds <0.4 m/s and colored according to fate (orange, re-impact; black, escape; red, orbiting Bennu within the Hill Sphere after 21 days).

Particle lifetime, and lifetime as a function of particle diameter, are important to consider for mission operations after TAG. Given the existence of a transient population of particles that could interfere with proximity operations, we wish to understand the residence lifetime(s) of

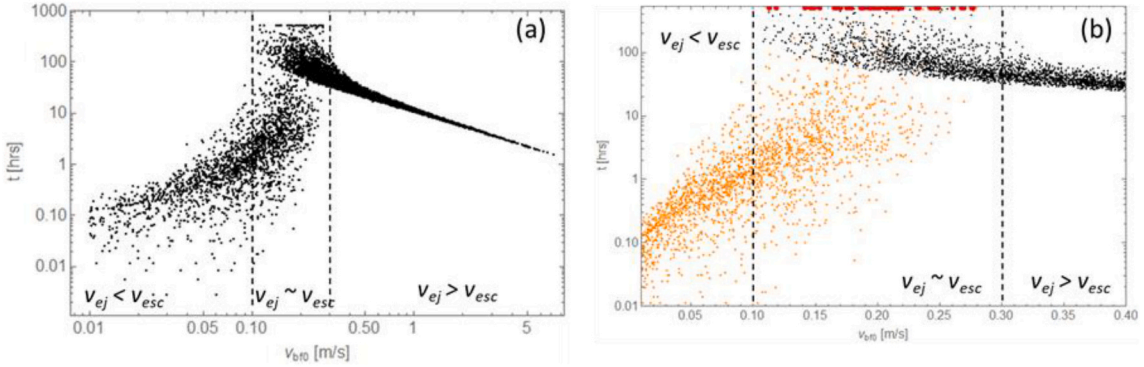

Fig. 16. Particle lifetime vs. body-fixed ejection velocity magnitude. (a) The complete simulated ejection-velocity range, with three regimes: (i) low velocities ($v_{ej} < v_{esc}$) corresponding to ballistic trajectories that re-impact Bennu; (ii) intermediate-velocity ($v_{ej} \sim v_{esc}$) trajectories that can re-impact Bennu, or escape, or remain in orbit (these have the longest lifetimes); and (iii) higher-velocity ($v_{ej} > v_{esc}$) trajectories that result in direct, hyperbolic escape. The maximum time possible is the 21-day (504-h) integration time. (b) The same data as in (a), focused on ejection speeds <0.4 m/s and colored to indicate particle fate: orange particles re-impact Bennu; black particles escape Bennu; red particles remain in orbit at the end of the simulation duration (21 days). All three fates exist for ejection speeds greater than 0.1 m/s and less than 0.3 m/s. (For interpretation of the references to colour in this figure legend, the reader is referred to the web version of this article.)

those particles. Fig. 17 illustrates the relationships between particle ejection speed, size, and trajectory duration. Fig. 17a plots initial ejection speed vs. particle diameter, using the same colour scheme as Fig. 16. The range of ejection speeds at a given diameter, and the decrease in maximum ejection speed with increasing particle size, reflect the assignment of initial velocity-magnitude values. Like Fig. 16, Fig. 17a shows that there is a velocity-magnitude range that corresponds to particles that remain in orbit for the 21-day simulation. Fig. 17b plots the fraction of ejected particles, in a given diameter bin, that remain in orbit after 21 days. The data show a decrease in lifetime as particle size decreases. Collectively, Fig. 17a and c illustrate the importance of SRP in the dynamics. Bennu's gravity is insufficient to retain small particles in orbit; SRP sweeps them away. SRP acceleration decreases as particle size increases (SRP is proportional to area-over-mass; area grows as r_p^2, while mass grows as r_p^3), reducing the capacity of SRP to strip a particle from orbit, even if initially SRP contributes to the particle reaching orbit (rather than impact or escape). Panels b and c of Fig. 17 constrain the particle population that could remain in orbit around Bennu for lifetimes

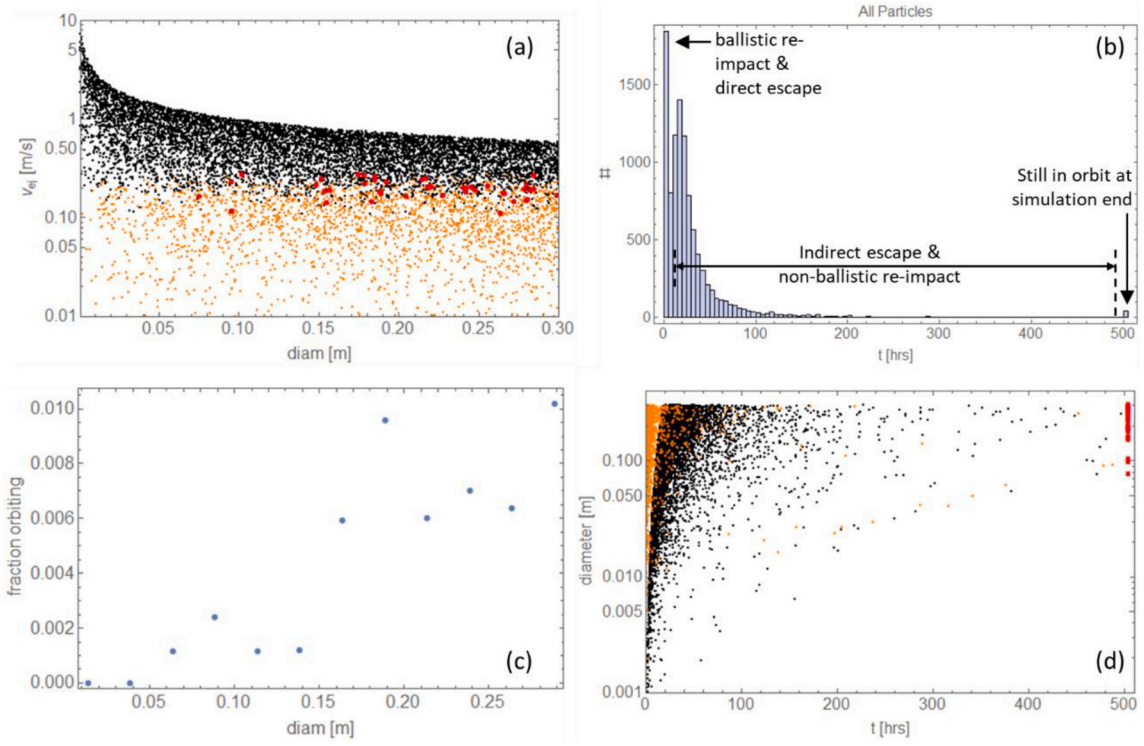

Fig. 17. Plots illustrating the effect of particle size on fate, and timing of fate, for a simulation of 10,000 particles. (a) Initial ejection velocity magnitude vs. diameter for the three types of particle fates: orange particles re-impact Bennu; black particles escape Bennu; red particles remain in orbit at the end of the simulation duration. (b) A histogram of particle lifetimes, showing three regimes: ballistic (or nearly so) re-impact and direct escape, non-ballistic re-impacts and indirect escapes that occur after one or more orbits, and particles still in orbit at the end of the simulation. Number of particles is shown on the y axis. (c) Fraction of particles, in a given size bin, that remain in orbit after 21 days. There is a decrease in survivability for smaller sizes (although the absolute values for all sizes are low). (d) Plot of diameter vs. particle lifetime, following the colour scheme of (a), that illustrates how the histogram in (b) divides into the subpopulations. (For interpretation of the references to colour in this figure legend, the reader is referred to the web version of this article.)

greater than the integration time reported here. Fig. 17b is a histogram of particle lifetimes from the simulation, where lifetime end is defined as either impacting Bennu, leaving the Hill Sphere, or remaining in orbit at the end of the simulation. The majority of particles have either re-impacted Bennu or escaped after 200 h. Fig. 17d plots particle diameter as a function of lifetime for each of the three subpopulations. Comparison with Fig. 16a and b shows that, as expected, the slowest and fastest ejection velocities are associated with the shortest lifetimes, those particles that re-impact or escape quickly. Particles continue to escape or re-impact Bennu up to the 21-day integration limit. As particle size increases, the fraction of those remaining in orbit at the end of the integration duration (21 days) also increases. Interestingly, McMahon et al. (2020) found that some simulated particles remained in orbit for over a year. The fact that such particles have not been observed to date could be due to either incomplete force modeling in the work described here and in Chesley et al. (2020) or McMahon et al. (2020), or could be due to observational biases in the particle imaging campaigns (Hergenrother et al. 2020).

We ran a second simulation (Fig. 18) with ejection speeds between 0.1 m/s and 0.3 m/s, which is the range that bounds the non-deterministic behavior of particle fate. Of the 10,000 simulated particles, 4180 re-impacted Bennu, 171 particles remained in orbit after the 21-day integration, and 5649 particles escaped. Fig. 19 is a set of histograms illustrating the relationships between launch angle and trajectory type. The left column contains histograms of the launch angle relative to local vertical (0° is vertical, 90° is horizontal), and the right column contains histograms of the launch direction relative to north (0° is north, 90° is east, 180° is south, 270° is west). The first row is for particles that re-impact Bennu, the second row is for particles that remain in orbit around Bennu, and the third row is for particles that escape.

The ejection angle relative to vertical is essentially uniform for particles that re-impact Bennu. There is an increase in the number of orbiting particles as this angle approaches 90° (as the particle is launched towards the horizon rather than "up"). These trajectories provide an increased opportunity for SRP to perturb the orbit prior to the next periapse. The slight increase in orbiting particles at these ejection angles decreases the number of particles that escape at similar angles.

The fate of the particle is more strongly dependent on ejection azimuth. Re-impact occurs more often when the rotation of Bennu acts to decrease the net ejection speed of a particle; this explains the peak in re-impacting particles around 270° azimuth. Conversely, particle escape is enhanced around 90° azimuth, where Bennu's rotation adds to the ejection speed received from the sample gas. For orbiting particles, there is a broad plateau in particle number between 100° and 310° azimuth.

These outcomes are, in part, a result of the ejection location on the sunward side of the asteroid. If the ejection location were nearer the terminator, or on the night side, the SRP effect would add to the particle velocity in the opposite sense than is demonstrated here.

3.3. Results from hypothetical TAG locations

The previous simulations provided an overview of the behavioral trends across velocity, diameter, ejection location, and ejection angles. In this section, we describe a second pair of simulations that targeted specific, though hypothetical, TAG sampling locations: one at high latitude (65°N), and one at the equator. In addition, the process for defining particle diameter changed to better reflect the expected inverse mass-velocity relationship seen during testing and the simulations, i.e., that more mass will be ejected at lower velocities.

Housen and Holsapple (2011) provide a comprehensive description of crater ejecta scaling laws. In terms of impactor properties, the amount of mass M ejected faster than a given velocity-magnitude v is:

$$\frac{M(v)}{m} = C_4 \left[\frac{v}{U} \left(\frac{\rho}{\delta} \right)^{\frac{3(\nu-1)}{3\mu}} \right]^{-3\mu} \tag{9}$$

where

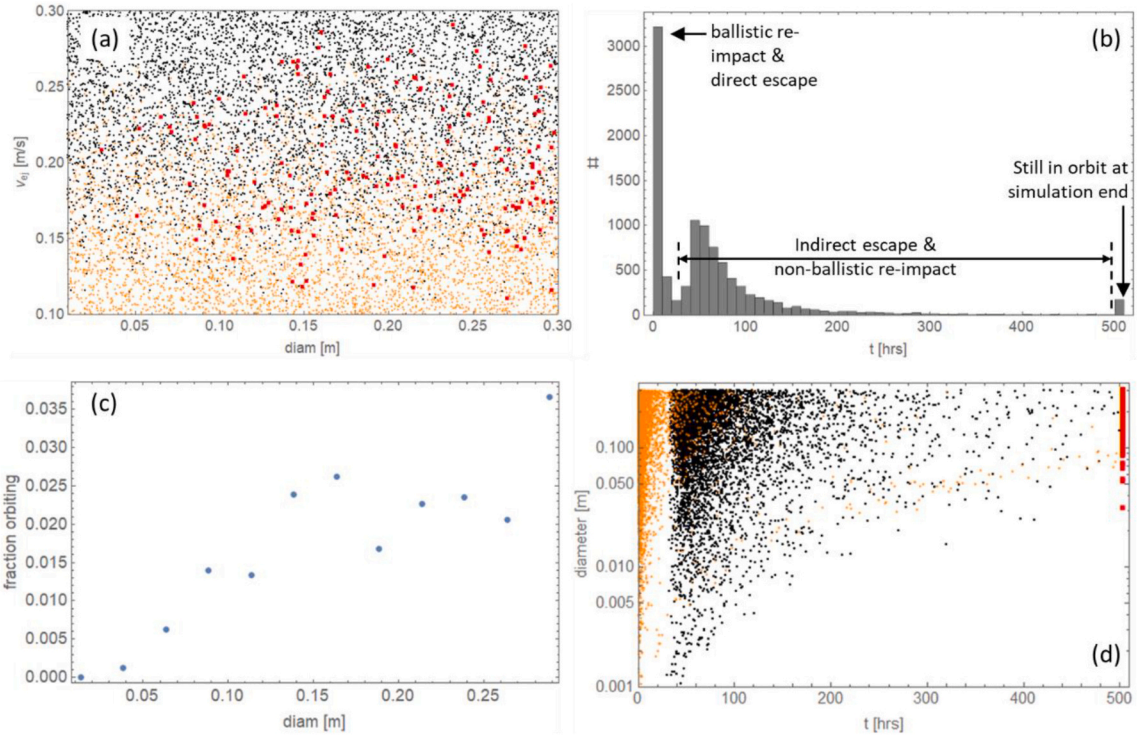

Fig. 18. Particles from the simulations with ejection velocity magnitudes restricted between 0.1 m/s and 0.3 m/s; see Fig. 17 for a description of the colors and plot formats. Because this simulation targets the range of ejection speeds that results in orbiting particles, the percent surviving is higher in this case than in the case that spans the full range of possible ejection speeds.

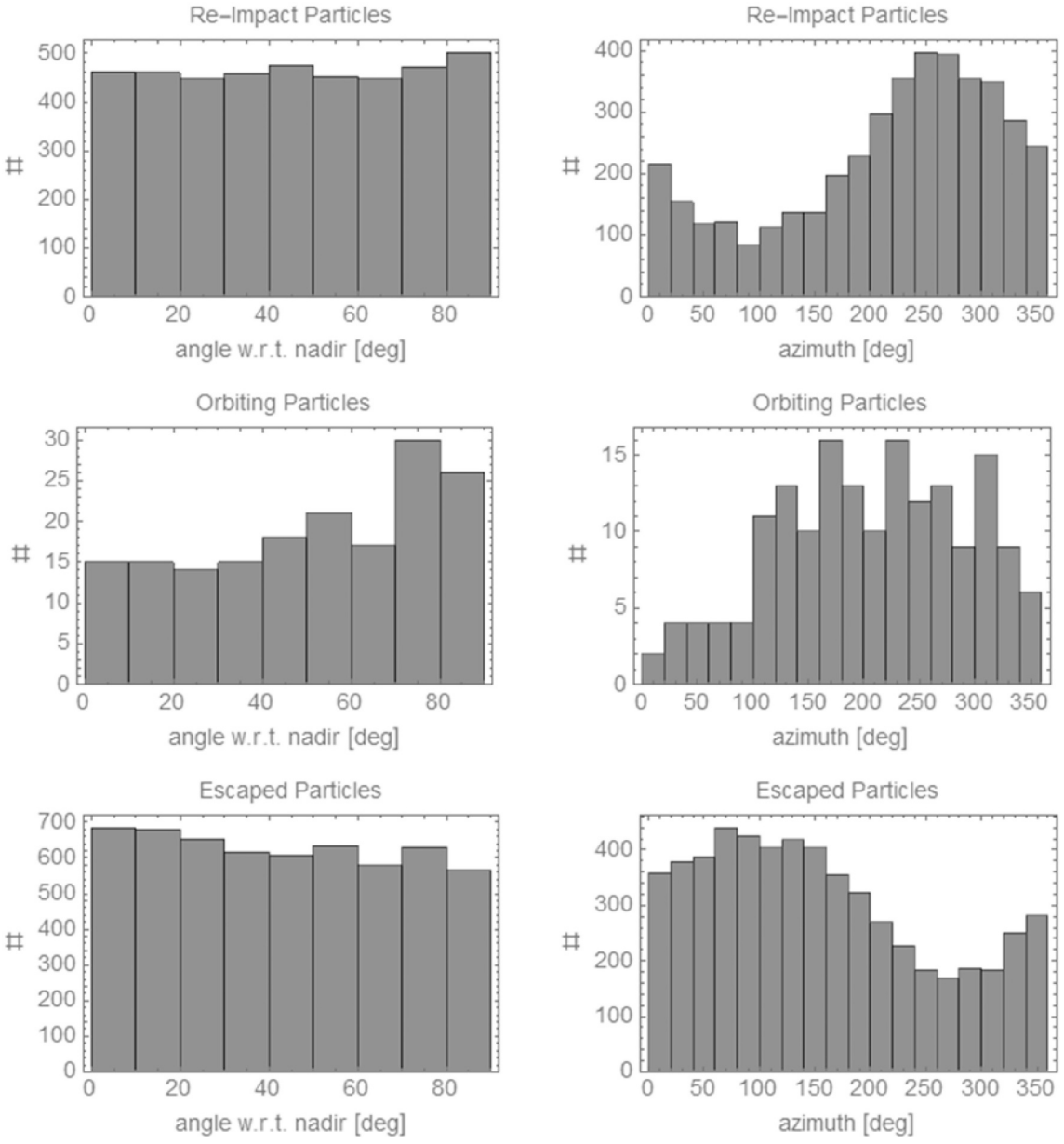

Fig. 19. Histograms to illustrate the correlation, or lack thereof, between particle fate and ejection angles. The top row is for re-impacting particles, the middle row is for orbiting particles, and the bottom row is for escaped particles. The left column is a histogram of the ejection angle with respect to (w.r.t.) vertical. At 0° the particle is ejected vertically; at 90° the particle is ejected horizontally. The right column is azimuthal angle, defined as clockwise from north. Thus, 90° is east, 180° is south, and 270° is west.

$$C_4 = \frac{3k}{4\pi} C_1^{3\mu} \tag{10}$$

and the other parameters are defined in Table 2 and Table 3. The same caveats articulated earlier, regarding the limitations of the crater-based analogy to TAGSAM-driven excavation, also apply to the derived velocities from these equations.

To generate particles for the simulation, first we determined the amount of mass expected within 0.01-m/s velocity-magnitude bins between 0.01 m/s and 0.3 m/s. This range includes, at its low end, trajectories that will re-accrete on Bennu, and it bounds the maximum non-deterministic behavior seen in the previous simulations. Then, for each velocity-mass bin, we created a population of particles whose diameters were calculated using a bounded Pareto distribution, which creates a power-law population between a minimum $d_{\min}$ and maximum $d_{\max}$ diameter:

$$d = \left(- \left(\frac{q d_{max}^b - q d_{min}^b - d_{max}^b}{d_{max}^b d_{min}^b} \right) \right)^{-1/b} \tag{11}$$

where q is randomly distributed between 0 and 1, and b is the absolute value of the power-law exponent for a differential power law. Bennu's boulders have a best-fit cumulative power-law exponent of -2.9 ± 0.3 (DellaGiustina et al., 2019), thus we used $b = 3.9$ (the differential exponent is one unit steeper than the cumulative exponent). Each particle created added to the mass for that velocity-magnitude bin. Once the particles created reached the total mass available in each bin, no further particles were generated for that velocity-magnitude bin. Thus, we had a realistic distribution of mass available in each velocity-magnitude bin, which was decomposed into a realistic distribution of particle sizes.

Fig. 20 plots the positions from the high-latitude and low-latitude

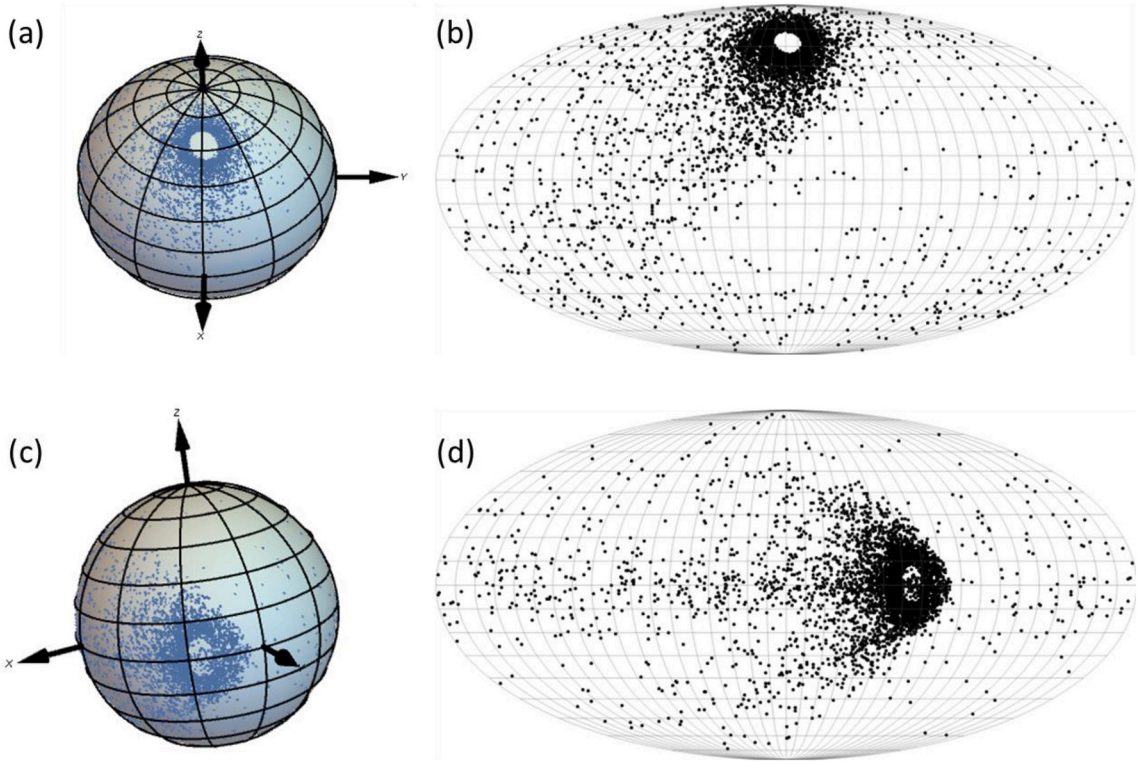

Fig. 20. Particle impact locations for the (a) high-latitude sample site, (b) Mollweide projection of the high-latitude site, (c) low-latitude sample site, and (d) Mollweide projection of the low-latitude site. For (a) and (c), latitude lines are plotted for every 15°, and longitude lines are plotted every 30°; for (b) and (d,) latitude and longitude lines are both plotted every 10°.

simulations. Panels (a) and (b) are renderings on a globe, and panels (c) and (d) are Mollweide projections. These plots illustrate the interplay between Bennu's rotation, the location of the TAG site, and the resulting ejecta patterns at regional and global scales. At high latitude, Bennu's surface speed is low enough that the asteroid does not rotate much underneath slow-moving ejecta, resulting in a roughly symmetric annular pattern created by the slow-moving ejecta. At the equator, however, Bennu's surface is moving fast enough that it rotates underneath the slowest-moving ejecta, resulting in an asymmetric impact annulus. In fact, the surface rotates underneath the lofted particles enough that the slowest-moving material, traveling towards the east, lands close to the original ejection point. The global distribution of impacts also expresses patterns in the impact locations caused by Bennu's rotation. In the high-latitude case, there is an underabundance of impacts to the southeast of the sample site. In the low-latitude case, there is an underabundance of impacts directly to the east of the sample site.

These simulations predict relative concentrations of impact locations, not absolute values. The total number of particles ejected by TAGSAM likely exceeds the simulated number of particles by a few orders of magnitude (parsing the ejected volume, described in Section 2.3, into a power-law population of particles corresponds to many more than simulated here), and thus re-impacting particles will be distributed across Bennu. These plots illustrate where concentrations of particle impacts will occur, or conversely, where particle impacts will be fewer than elsewhere.

4. Predictions and implications

4.1. Predictions for the OSIRIS-REx TAG sampling event

The tests and simulations provide a basis for predicting the mass ejected during TAG, the distribution of velocities, and the fate of the particles ejected as a function of velocity. In turn, these results inform operational expectations for the mission after TAG.

TAG site effects. The transfer of sample-gas potential energy to kinetic energy of particles on Bennu's surface will mobilize material beyond the amount of material collected by TAGSAM. Contact duration between TAGSAM and the surface will determine the amount of energy transfer between the gas bottle and the surface. If all, or nearly all, of the energy of the bottled gas is deposited into the surface, the TAG event should leave a crater-like feature on Bennu's surface. The size and depth of the crater is strongly dependent on Bennu's unknown surface properties. If we assume a low cohesive strength (nearly zero), and if we approximate the crater-like feature as a paraboloid of revolution with an assumed depth of 20% of the diameter, using an ejected volume of 0.12 m^3 (the volume ejected from one of the low-density collection tests), the feature could be up to 1.2 m diameter and over 20 cm deep. If there is layering with a discrete boundary to a stronger (more cohesive) layer in the near subsurface, the excavated depth may extend only so far as that layer boundary (see Schultz et al., 2007).

Distribution of re-impact particles. The greatest concentration of ejecta will land near the TAG site. However, particle re-impact will occur across Bennu; in both cases shown in Fig. 20, the reach of ejected material is essentially global. A low-latitude TAG site results in the largest asymmetry in the ejecta distribution, caused by the speed of Bennu rotating underneath the slow-moving ejecta that re-impacts Bennu. As TAG site latitude increases, the asymmetry will be less pronounced.

The center of the primary OSIRIS-REx TAG site, Nightingale (Fig. 1), is at approximately 56.0° N latitude and 42.1° E longitude; the center of the backup TAG site, Osprey, is at approximately 11.6° N latitude and 88.9° E longitude. The latitudes of these sites are similar to the latitudes of the two hypothetical TAG sites in Section 3.3. Fig. 21 plots the ratio of Bennu's surface speed to the total particle ejection speed (where the total speed is the combination of the gas-induced speed and Bennu's rotation) as a function of latitude and ejection speed. This plot indicates

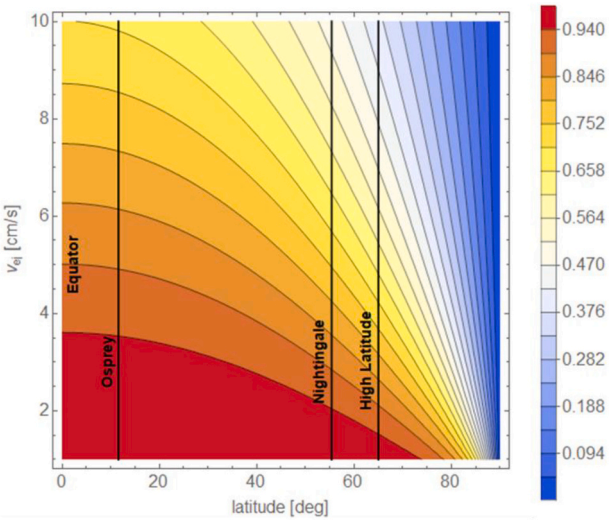

Fig. 21. The ratio of Bennu's surface speed to the total particle speed (where the total particle speed is gas ejection speed plus Bennu's surface speed), as a function of latitude and gas ejection speed (v_{ej}). The calculation assumes Bennu is a sphere with radius of 245 m and rotation period of 4.296 h. Vertical lines correspond to hypothetical high- and low-latitude (at the equator) TAG sites described in Section 3.3, as well as the mission's actual primary and backup TAG sites, Nightingale and Osprey, respectively.

that, although there are differences in the velocity-magnitude ratios between the hypothetical and actual TAG sites, we can expect similar behavior between the high-latitude TAG site and Nightingale, as well as between the low-latitude TAG site and Osprey.

Lifetime of ejected particles. Fig. 17 and Fig. 18 illustrate that the particle population resident around Bennu initially decays rapidly as the slowest-moving particles re-impact Bennu, and the fastest-moving escape. There is a secondary peak at ~1 day of particle lifetime (Fig. 17b) caused by a population of particles that achieve short-lived orbits around Bennu; some of these re-impact Bennu, but most of them escape (Fig. 17d). After 200 h (8.3 days), only a few percent of the particles remain. There is further decay of particles via both re-impact and escape until the end of the 21-day simulation duration.

4.2. Implications for crater ejecta and regolith mobility

The testing of TAGSAM using low-density simulants demonstrated an inverse mass-velocity relationship for ejected material; this behavior is consistent with classical impact-crater ejecta and is the motivation for developing a crater-ejecta–like model for TAGSAM ejecta. Given the similarity between the two ejection processes, the results from modeling specific, hypothetical TAG site locations (Fig. 20) inform expectations for the behavior of crater ejecta on Bennu.

A notable outcome of the two simulations shown in Fig. 20 is the different spatial distribution of the slow-moving ejecta. The low-latitude case exhibits an east-west asymmetry caused by the rotation of Bennu, whereas the high-latitude case is more uniform. Because the effect is a function of latitude, one would expect the morphology of craters to progress between the two states as an impact site increases in latitude. The extensive, high-resolution imaging by OCAMS (Rizk et al., 2018) and global, high-resolution lidar coverage by OLA (Daly et al., 2017) provide the necessary data sets to investigate whether a rotationally produced asymmetry exists for crater ejecta.

The larger-scale spatial patterns of ejecta locations have consequences for understanding the distribution of ejected material from an impact location. On larger bodies, barring highly oblique impacts, low-speed crater ejecta extends in a roughly symmetrical distribution, creating the ejecta blanket immediately surrounding the crater. Higher-speed ejecta forms discrete rays that may not be uniform like an ejecta blanket, yet still are generally distributed around the crater. In the microgravity of Bennu, only very-low-speed ejecta is retained deterministically; even 10-cm/s material can escape under the right conditions. To return to the surface as a continuous ejecta blanket surrounding the source crater, the ejecta must move only 2 to 3 cm/s at most. If there is a minimum ejecta speed on Bennu, then there is a minimum diameter crater with a continuous ejecta blanket; ejecta produced from smaller craters will land too far away to be identified as a continuous ejecta blanket. Fig. 22 illustrates this concept. Assume s is the distance traveled by ejecta particle launched at v_{min}, the smallest ejection speed permitted by Bennu's regolith. Craters with radius near s or larger will have a continuous ejecta blanket because the last ejected material falls just outside the crater rim. As crater radius decreases, the crater rim moves farther away from the impact range of the slowest-ejected material. Other aspects of crater formation related to the mobilization of material, e.g., the formation of crater rims by lateral flow, could also be constraints on cohesive properties of Bennu's surface.

If there is a minimum-diameter crater with evidence for a continuous ejecta blanket–like feature, that implies a cohesive value in the regolith that halts material ejection, which would be an important parameter for understanding all types of regolith mechanics and dynamics. On the other hand, if continuous ejecta blankets exist at the smallest observable sizes, that implies a near-strengthless regolith, at least for the material to the depth excavated by the impact.

When considered in conjunction with Fig. 20 and Fig. 21 (the effect of rotation on ejecta), investigation of crater ejecta could provide constraints on both the cohesion of Bennu's regolith as well as Bennu's rotation. If Bennu's spin rate has changed over the lifetime of accumulating impact craters, that signature should be present in different asymmetries of crater ejecta blankets at the same latitude. This assumes evidence of an ejecta blanket is visible in one or more of the OSIRIS-REx data sets.

Similarly, Fig. 14 provides a notable outcome for particle mobility on Bennu, namely that the particle sizes that are most easily moved are tens of cm to nearly a meter in size. Particle mobility as a function of size has several significant implications for the behavior of re-accreted ejecta, the response of surface material to seismic shaking or other sources of external energy (YORP spin-up, tidal effects during close planetary flybys). Movement of material, and erosion of surface features, may be dominated by objects nearly 1 m diameter. This is an example of the unique behavior of particles in a micro-gravity environment that is counter-intuitive to Earth-based experience.

Finally, there are some interesting implications for the physical processing of material that is retained on Bennu and the nature of the sample that OSIRIS-REx will return. An impact deposits a substantial amount of energy in a short period of time, which causes high pressures and temperatures in a volume within the impact site, creating shock-processed material that differs from the unprocessed target material. Typically much of this material is then excavated at speeds that would be sufficient to escape Bennu. Material ejected at a later stage receives sufficient energy for excavation but is not subject to high pressures or temperatures. Porous targets tend to reduce peak pressures from impact and depress ejecta speeds (e.g. Housen et al., 2018). It is possible there is a fractionation mechanism on Bennu (and for other small asteroids as well) in which the most impact-processed material from an impact tends to escape, whereas the least impact-processed material, on average, is retained. The magnitude of this fractionation depends on details — such as the porosity's effects on the impactor and peak pressures — that are not yet well known. Indeed, we do not conclude that impact-processed material is absent on Bennu: meteoroid impacts make small, localized shock volumes in individual rocks that remain on the surface Ballouz et al. (2020), and it is possible that some fraction of Bennu is shocked material that reaccumulated into the asteroid from its parent body. Nevertheless, the returned sample from Bennu may include material that is not significantly shock-processed.

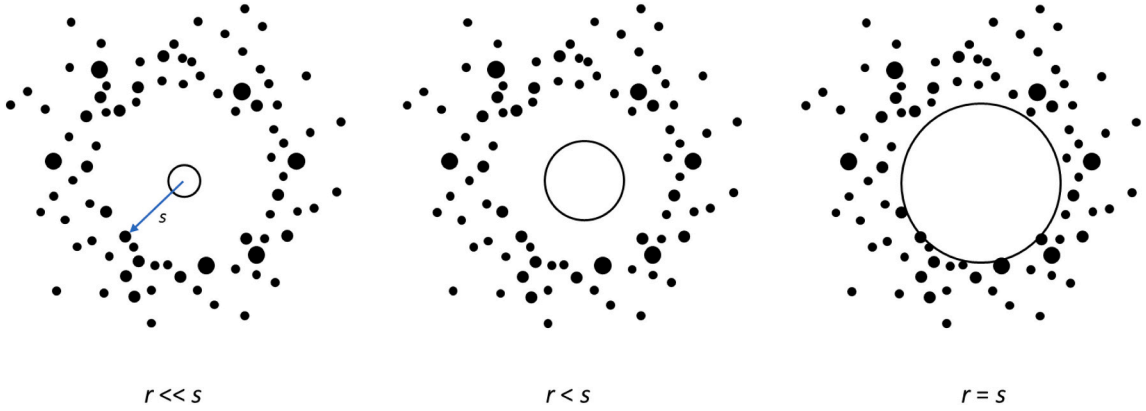

Fig. 22. Schematic illustrating the effect of a minimum possible ejection speed and the corresponding geometry between the crater rim and the impact locations of the slowest-moving ejecta. When crater radius r is less than the minimum distance s traveled by an ejecta launched with v_{min}, the crater will not have a continuous ejecta blanket, or the asteroid-regolith equivalent.

4.3. Implications for natural particle ejection mechanism(s)

Lauretta and Hergenrother et al. 2019 report on multiple small-particle ejection events from Bennu's surface. They posit that the most plausible ejection mechanisms include thermal fracturing, volatile release by dehydration of phyllosilicate rocks, and meteoroid impacts — or perhaps some combination of those mechanisms. Observed particle velocities range from 6 cm/s to over 3.3 m/s, and estimated ejection energies range between 8 mJ and 270 mJ. Particles either reimpact the surface or escape on hyperbolic trajectories. Particles that reimpact either travel on short suborbital arcs or reside in transient orbits from 2 to 6 days.

Several features of the observed particle population reported by Lauretta et al., 2019b are present in the results described here. The surface-relative velocities of the particles that achieve temporary orbit range from 10 to 25 cm/s, consistent with simulation data shown in Fig. 16. The lifetime of 2 to 6 days for these particles is consistent with the secondary peak in the histogram shown in Fig. 17b. We conclude that our simulations, covering ~98% of the modeled accelerations reported in Chesley et al. (2020) and McMahon et al. (2020), are sufficient to capture the short-term behavior of ejected particles.

We use that similarity to infer characteristics of the real particle ejection events from Bennu. There is a comparable range of observed ejection velocities between the real ejected particles (Lauretta et al. (2019b) report naturally-ejected particle speeds of ~0.05 to >3 m/s) and the simulation data in Fig. 16 and Fig. 18. *Re*-accumulation of slow-moving ejecta should follow the pattern of symmetric near the poles to asymmetric near the equator (e.g., Fig. 20 and Fig. 21) because of the relative magnitudes of particle ejection speed and Bennu's rotation speed. In our simulations, which include a broad range of ejection velocity and latitude, the efficiency for achieving orbit is low: over the course of the full 21-day integration, 42% re-impact Bennu, 56% escape, and up to 2% are still in orbit. Fig. 23 plots the percentages of re-impact, orbit, and escape populations vs. ejection speed for the data sets shown in Fig. 16 and Fig. 18. In both cases, escape becomes the majority outcome at ~18 cm/s. Mass loss estimates of this process should consider the number, sizes, and ejection speeds of ejected particles.

Because the timescale associated with particle movement caused by ejection events is short — days to weeks — the process likely is one of the fastest methods of particle transport across the surface, at least for small particles. The current absence of any visible or spectral correlation of particle re-accretion in discrete areas across Bennu's surface implies that the locations of ejection events are distributed across the surface and not concentrated in a few areas, consistent with the findings of Chesley et al. (2020).

For particles that achieve transient orbits, there is an orbital survival efficiency as a function of diameter (Fig. 17c and Fig. 18c); larger particles are more likely to survive in orbit for longer periods of time. During the approach to Bennu, OSIRIS-REx conducted a satellite survey and did not find anything larger than 10 cm in orbit around Bennu (Hergenrother et al. 2019). The absence of particles that size and larger in longer-term orbits suggests that it is rare for natural particle ejection events to have sufficient energy to launch ≥10-cm particles that achieve orbit.

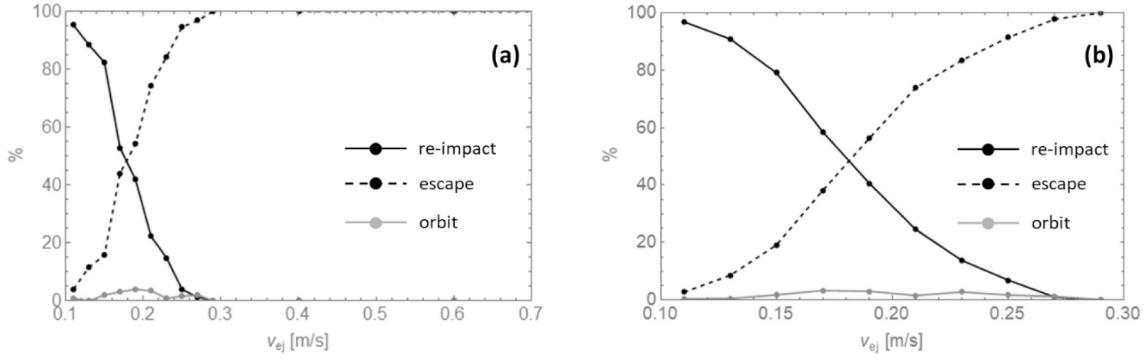

Fig. 23. Simulated ejected particles, binned into 0.02 m/s ejection velocity-magnitude bins, and grouped according to fate. (a) For data shown in Fig. 16 (ejection speeds up to 7 m/s, although the plot range is for speeds ≤0.7 m/s, at higher speeds all ejecta escapes). (b) For data shown in Fig. 18 (ejection speeds limited between 0.1 and 0.3 m/s). The solid black line is for particles that re-impact Bennu, the solid gray line is for particles that remain in orbit at the end of the integration duration, and the dashed black line is for particles that escape.

5. Conclusions

We conducted a suite of complementary ground-based tests and numerical simulations to predict the amount, speeds, distribution, and fate of material mobilized by the OSIRIS-REx sampling apparatus, TAGSAM. Based on our results, we expect the following outcomes from the sample collection event:

- The total mass of material mobilized by the TAGSAM gas could range from 12 kg to at least 165 kg; this range is expected to span the uncertainties in Bennu's properties and in the assumed values used for our modeling. The larger masses correspond to weaker cohesive strengths and are the more likely outcome, given that Bennu is a rubble pile and considering that Arakawa et al. (2020) derive a < 1.3 Pa cratering strength for Ryugu.
- Some of the mobilized material will be ejected at maximum speeds of up to 10 m/s.
- Any material moving faster than 30 cm/s will escape Bennu.
- Material ejected at speeds between 10 cm/s and 30 cm/s may or may not escape Bennu, depending ejection direction, ejection location, and speed.
- Material ejected at speeds less than 10 cm/s will re-accrete on Bennu. Given an inverse mass–velocity magnitude relationship for the ejecta, much of the material will land regionally near the TAG site, although because of Bennu's low gravity, some material will be distributed globally.
- Some of the ejected material will remain in transient orbits around Bennu. The lifetimes of these orbits could span from days to at least several weeks, the maximum duration of our integrations.
- Gas from TAGSAM likely will mobilize material beyond the contact location. There is a preferred particle size for mobility, between 50 and 80 cm, depending on the TAG site latitude. Smaller particle sizes are resistant to gas pressure via cohesion, while larger sizes are resistant to gas pressure via gravity. This is an outcome that could link erosion and particle sorting on rubble piles to natural sources of external energy input (e.g., seismic shaking, YORP spin-up, tidal forces).

Data availability

Data that are the basis for Fig. 16, Fig. 18, Fig. 20, and Fig. 23 are available on request.

Declaration of Competing Interest

None

Acknowledgements

This material is based upon work supported by NASA under Contracts NNG12FD66C and NNM10AA11C issued through the New Frontiers Program. We are grateful to the entire OSIRIS-REx Team for making the encounter with Bennu possible. BR acknowledges funding support from the Royal Astronomical Society (RAS) and the UK Science and Technology Facilities Council (STFC).

References

Alvarellos, J.L., Zahnle, K.J., Dobrovolskis, A.R., Hamill, P., 2002. Orbital evolution of impact Ejecta from Ganymede. Icarus 160, 108–123.
Alvarellos, J.L., Zahnle, K.J., Dobrovolskis, A.R., Hamill, P., 2005. Fates of satellite ejecta in the Saturn system. Icarus 178, 104–123.
Anderson, J.L.B., Schultz, P.H., Heineck, J.T., 2003. Asymmetry of ejecta flow during oblique impacts using three-dimensional particle image velocimetry. J. Geophys. Res. 108 https://doi.org/10.1029/2003JE002075.
Arakawa, M., Saiki, T., Wada, K., Ogawa, K., Kadona, T., Shirai, K., Sawada, H., Ishibashi, K., et al., 2020. An artificial impact on the asteroid 162173 Ryugu formed a crater in the gravity-dominated regime. Science. https://doi.org/10.1126/science.aaz1701.
Ballouz, Ronald, 2017. Numerical Simulations of Granular Physics in the Solar System. University of Maryland, College Park, PhD Dissertation.
Ballouz, R.-L., Walsh, K.J., Barnouin, O.S., DellaGiustina, D.N., Al Asad, M., Jawin, E.R>, Daly, M.G., Bottke, W.F., Michel, P., Avdellidou, C., Delbo, M., Daly, R.T., Asphaug, A., Bennett, C.A., Bierhaus, E.B., Connolly, H.C., Golish, D.R., Molaro, J.L., Nolan, M. C., Pajola, M., Rizk, B., Schwartz, S.R., Trang, D., Wolner, C.W.V., and Lauretta, D.S. (in press) Bennu's near-Earth lifetime of 1.75 million years inferred from craters on its boulders. Nature (2020). DOI: 10.1038/s41586-020-2846-z.
Barnouin, O.S., et al., 2019. Shape of (101955) Bennu indicative of a rubble pile with internal stiffness. Nat. Geosci. 12, 247–252.
Bart, G.D., Melosh, H.J., 2010. Distributions of boulders ejected from lunar craters. Icarus 209, 337–357.
Bierhaus, E.B., Dones, L., 2015. Craters and ejecta on Pluto and Charon: anticipated results from the new horizons flyby. Icarus 246, 165–182.
Bierhaus, E.B., Clark, B.C., Harris, J.W., Payne, K.S., Dubisher, R.D., Wurts, D.W., Hund, R.A., Kuhns, R.M., Linn, T.M., Wood, J.L., May, A.J., Dworkin, J.P., Beshore, E., Lauretta, D.S., 2018. The OSIRIS-REx spacecraft and the touch-and-go sample acquisition mechanism (TAGSAM). Space Sci. Rev. 214 (7) article id. 107.
Bottke, W.F., Moorehead, A., Connolly Jr., H.C., Hergenrother, C.W., Molaro, J.L., Michel, P., Nolan, M.C., Schwartz, S.R., Vokrouhlicky, D., Walsh, K.J., Lauretta, D.S., 2020. Meteoroid impacts as a source of Bennu's particle ejection events. JGR Planets. https://doi.org/10.1029/2019JE006282.
Brack, D.N., McMahon, J.W., 2019. Modeling the coupled dynamics of an asteroid with surface boulder motion. Icarus 333, 96–112.
Brisset, J., Colwell, J., Dove, A., Abukhalil, S., Cox, C., Mohammed, N., 2018. Regolith behavior under asteroid-level gravity conditions: low-velocity impact experiments. Progr. Earth Planet. Sci. 5 https://doi.org/10.1186/s40645-018-0222-5.
Chabai, A.J., 1977. Influence of gravitational fields and atmospheric pressures on scaling of explosion craters. Impact and Explosion Cratering. Pergamon Press, New York, pp. 1191–1214.
Chesley, S.R., French, A.S., Davis, A.B., Jacobson, R.A., Brozović, M., Farnocchia, D., Selznick, S., Liounis, A.J., Hergenrother, C.W., Moreau, M.C., Pelgrift, J., Lessac-Chenen, E., Molaro, J.L., Park, R.S., Rozitis, B., Scheeres, D.J., Takahashi, Y., Vokrouhlický, D., Wolner, C.W.V., Adam, C., Bos, B.J., Christensen, E.J., Emery, J.P., Leonard, J.M., McMahon, J.W., Nolan, M.C., Shelly, F.C., Lauretta, D.S., 2020. Trajectory estimation for particles observed in the vicinity of (101955) Bennu. JGR Planets. https://doi.org/10.1029/2019JE006363.
Cintala, M.J., Berthoud, L., Hörst, F., 1999. Ejection-velocity distributions from impacts into coarse-grained sand. Meteorit. Planet. Sci. 34, 605–623.
Clark, B.C., Bierhaus, E.B., Harris, J.W., Payne, K.S., Wurts, D.W., Dubisher, R.D., Deden, S.L., 2016. TAGSAM: A gas-driven system for collecting samples from solar system bodies. IEEE Aerospace Conference, Big Sky, MT (March, 2016). https://doi.org/10.1109/AERO.2016.7500871.
Colwell, J.E., 2003. Low velocity impacts into dust: results from the COLLIDE-2 microgravity experiment. Icarus 164, 188–196.
Colwell, J.E., Gulbis, A.A.S., Horanyi, M., Robertson, S., 2005. Dust transport in photoelectron layers and the formation of dust ponds on Eros. Icarus 175, 159–169.
Colwell, J.E., Sture, S., Cintala, M., Durda, D., Hendrix, A., Goudie, T., Curtis, D., Ashcom, D.J., Kanter, M., Keohane, T., Lemos, A., Lupton, M., Route, M., 2008. Ejecta from impacts at 0.2 2.3 m/s in low gravity. Icarus 195, 908–917.
Cooper, M.R., Kovach, R.L., Watkins, J.S., 1974. Lunar Near-Surface Structure. Rev. Geophys. Space Phys. 12, 291–308.
Daly, M.G., Barnouin, O.S., Dickinson, C., Seabrook, J., Johnson, C.L., Cunningham, G., Haltigin, T., Gaudreau, D., Brunet, C., Aslam, I., Taylor, A., Bierhaus, E.B., Boynton, W., Nolan, M., Lauretta, D.S., 2017. The OSIRIS-REx laser altimeter (OLA) investigation and instrument. Space Sci. Rev. 212, 899–924.
DellaGiustina, D.N., Emery, J.P., et al., 2019. Properties of rubble-pile asteroid (101955) Bennu from OSIRIS-REx imaging and thermal analysis. Nature Astronomy 3, 341–351.
Emery, J.P., Fernande, Y.R., Kelley, M.S.P., Warden, K.T., Hergenrother, C., Lauretta, D. S., Drake, M.J., Campins, H., Ziffer, J., 2014. Thermal infrared observations and thermophysical characterization of OSIRIS-REx target asteroid (101955) Bennu. Icarus 234, 17–35.
Greeley, R., Iversen, J.D., 1985. Wind as a Geological Process on Earth, Mars, Venus, and Titan. Cambridge University Press, New York.
Hartzell, C.M., Scheeres, D.J., 2011. The role of cohesive forces in particle launching on the moon and asteroids. Planet. Space Sci. 59, 1758–1768.
C.W. Hergenrother1, C.K. Maleszewski1, M.C. Nolan 1, J.-Y. Li 2, C.Y. Drouet d'Aubigny1, F.C. Shelly1, E.S. Howell1, T.R. Kareta 1, M.R.M. Izawa3, M.A. Barucci 4, E.B. Bierhaus5, H. Campins6, S.R. Chesley7, B.E. Clark 8, E.J. Christensen1, D.N. DellaGiustina1, S. Fornasier 4, D.R. Golish 1, C.M. Hartzell9, B. Rizk1, D.J. Scheeres10, P.H. Smith1, X.-D. Zou2, D.S. Lauretta 1 & The OSIRIS-REx Team (2019). The operational environment and rotational acceleration of asteroid (101955) Bennu from OSIRIS-REx observations. Nature Communications, v. 10, doi: 10.1038/s41467-019-09213-x.
Holsapple, K.A., 1993. The scaling of impact processes in planetary sciences. Annu. Rev. Earth Planet. Sci. 21, 333–373.
Housen, K.R., Holsapple, K.A., 2011. Ejecta from impact craters. Icarus 211, 856–875.
Housen, K.R., Sweet, W.J., Holsapple, K.A., 2018. Impacts into porous asteroids. Icarus 300, 72–96.
Kok, J.F., Parteli, E.J.R., Michaels, T.I., Karam, D.B., 2012. The physics of wind-blown sand and dust. Rep. Progr. Physics 75, 72 pp.
Lauretta, D.S., Balram-Knutson, S.S., Beshore, E., Boynton, W.V., Drouet d'Aubigny, C., DellaGiustina, D.N., Enos, H.L., Gholish, D.R., Hergenrother, C.W., Howell, E.S.,

Johnson, C.A., Morton, E.T., Nolan, M.C., Rizk, B., Roper, H.L., Bartels, A.E., Bos, B. J., Dworkin, J.P., Highsmith, D.E., Moreau, M.C., Lorenz, D.A., Lim, L.F., Mink, R., Nuth, J.A., Reuter, D.C., Simon, A.A., Bierhaus, E.B., Bryan, B.H., Ballouz, R., Barnouin, O.S., Binzel, R.P., Bottke, W.F., Hamilton, V.E., Walsh, K.J., Chesley, S.R., Christensen, P.R., Clark, B.E., Connolly, H.C., Crombie, M.K., Daly, M.G., Emery, J. P., McCoy, T.J., McMahon, J.W., Scheeres, D.J., Messenger, S., Nakamura-Messenger, K., Righter, K., Sandford, S.A., 2017. OSIRIS-REx: sample return from asteroid (101955) Bennu. Space Sci. Rev. 212, 925–984.

Lauretta, D.S., DellaGiustina, D.N., et al., 2019a. The unexpected surface of asteroid (101955) Bennu. Nature 568, 55–60.

Lauretta, D.S., Hergenrother, C.W., et al., 2019b. Episodes of particle ejection from the surface of the active asteroid (101955) Bennu. Science 366 article id eaay3544.

McMahon, J.W., Scheeres, D.J., Chesley, S.R., French, A., Brack, D., Farnocchia, D., Takahashi, Y., Tricarico, P., Mazarico, E., Bierhaus, B., Hergenrother, C.W., Lauretta, D.S., 2020. Dynamical evolution of simulated particles ejected from asteroid Bennu. JGR Planets. https://doi.org/10.1029/2019JE006229.

Molaro, J.L., et al., 2020. Thermal fatigue as a driving mechanism for activity on asteroid Bennu. JGR Planets. https://doi.org/10.1029/2019JE006325.

Molaro, J.L., Walsh, K.J., Jawin, E.R., Ballouz, R.-L., Bennet, C.A., Golish, D.R., d'Aubigny, C.D., DellaGiustina, D.N., Rizk, B., Schwartz, S.R., Delbo, M., Hanna, R. D., Pajola, M., Campins, H., Ryan, A.J., Bottke, W.F., Lauretta, D.S., 2020a. In-situ evidence of thermally induced rock breakdown widespread on Bennu's surface. Nat. Commun. 11 article id 2913.

Nolan, M.C., Magri, C., Howell, E.S., Benner, L.A.M., Giorgini, J.D., Hergenrother, C.W., Hudson, R.S., Lauretta, S.S., Margot, J.L., Ostro, S.J., Scheeres, D.J., 2013. Shape model and surface properties of the OSIRIS-REx target asteroid (101955) Bennu from radar and lightcurve observations. Icarus 266, 629–640.

Nordyke, M.D., 1962. An analysis of cratering data from desert alluvium. J. Geophys. Res. 67, 1965–1974.

Oberbeck, V.O., 1971. Laboratory simulation of impact cratering with high explosives. J. Geophys. Res. 76, 5732–5749.

Oberbeck, V.O., 1975. The role of ballistic Erosion and sedimentation in lunar stratigraphy. Rev. Geophys. Space Phys. 13, 337–362.

Oelze, M.L., O'Brien, W.D., Damody, R.G., 2002. Measurement of attenuation and speed of sound in soils. Soil Sci. Soc. Am. J. 66, 788–796.

Rizk, B., d'Aubigny, C., Golish, D., Fellows, C., Merrill, C., Smith, P., Walker, M.S., Hendershot, J.W., Hancock, J., DellaGiustina, D., Tanner, R., Williams, M., Harshman, K., Fitzgibbon, M., Verts, W., Chen, J., Dowd, A., Read, M., Hamara, D., Connors, T., Burt, R., Whiteley, M., Watson, M., Crowther, B., McMahon, T., Lowman, A., Harrison, L., Williams, B., Hunten, M., Little, E., Ward, M., Booher, D., Saltzman, T., Alfred, D., O'Dougherty, S., Walthall, M., Kenagy, K., Peterson, S., See, C., Selznick, S., Suave, C., Beiser, M., Lancaster, A., Black, W., Lauretta, D., Oliver, S., Morgan, C., Oquest, C., Crowley, D., Castle, C., Dominguez, R., Sullivan, M., 2018. OCAMS: the OSIRIS-REx camera suite. Space Sci. Rev. 214 article id 26.

Rozitis, B., Emery, J.P., Siegler, M.A., Susorney, H.C.M., Molaro, J.L., Hergerother, C.W., Lauretta, D.S., 2020. Implications for ice stability and particle ejection from high-resolution temperature modeling of asteroid (101955) Bennu. Journal of Geophysical Research: Planets 125. https://doi.org/10.1029/2019JE006323 e2019JE006323.

Sanchez, P., Scheeres, D.J., Bierhaus, E.B., Clark, B., 2013. Simulations of Regolith Interactions in Microgravity. 44th Lunar and Planetary Science Conference 2271. LPI Contribution No. 1719.

Scheeres, D., 2012. Orbital Motion in Strongly Perturbed Environments, Applications to Asteroid. Springer Press, Comet and Planetary Satellite Orbiters. ISBN 978-3-642-03256-1.

Scheeres, D.J., Hartzell, C.M., Sanchez, P., Swift, M., 2010. Scaling forces to asteroid surfaces: the role of cohesion. Icarus 210, 968–984.

Scheeres, D.J., et al., 2019. The dynamical geophysical environment of (101955) Bennu based on OSIRIS-REx measurements. Nature Astronomy 3, 352–361.

Scheeres, D.J., McMahon, J.W., Brack, D.N., French, A.S., Chesley, S.R., Farnocchia, D., Vokrouhlicky, D., Ballouz, R.-L., Emery, J.P., Rozitis, B., Nolan, M.C., Hergenrother, C.W., Lauretta, D.S., 2020. Particle ejection contributions to the rotational acceleration and orbit evolution of asteroid (101955) Bennu. JGR Planets. https://doi.org/10.1029/2019JE006284.

Schultz, P.H., 1992. Atmospheric effects on Ejecta emplacement. J. Geophys. Res. 97, 11,623–11,662.

Schultz, P.H., Gault, D.E., 1985. Clustered impacts: experiments and implications. J. Geophys. Res. 90, 3701–3732.

Schultz, P.H., Eberhardy, C.A., Ernst, C.M., A'Hearn, M.F., Sunshine, J.M., Lisse, C.M., 2007. The deep impact oblique impact cratering experiment. Icarus 191, 84–122.

Tancredi, G., Roland, S., Bruzzone, S., 2015. Distribution of boulders and the gravity potential on asteroid Itokawa. Icarus 247, 279–290.

Tatsumi, E., Sugita, S., 2018. Cratering efficiency on coarse-grained targets: implications for the dynamical evolution of asteroid 25143 Itokawa. Icarus 300, 227–248.

Teramoto, K., Yano, H., 2005. Measurements of Sound Speed in Granular Materials Simulated Regolith. LPSC XXXVI, abstract no. 1856.

Vickery, A.M., 1986. Size-velocity distribution of large ejecta fragments. Icarus 67, 224–236.

Yuichi, T., Takanao, S., Terui, F., Nakazawa, S., Yoshikawa, M., Watanabe, S., the Hayabusa2 Project Team, 2020. Hayabusa2 mission status: landing, roving and cratering on asteroid Ryugu. Acta Astronautica 171, 42–54.